TOWARDS 3D DIRECT CURRENT RESISTIVITY AND INDUCED POLARIZATION
IMAGING

by

Kun Guo

A research report submitted in conformity with the requirements
for the degree of Master of Science
Graduate Department of Earth Sciences
University of Toronto

Executive Summary

In this report, I investigate the capability of direct current resistivity and induced polarization (DC/IP) method in time lapse monitoring and three dimensional imaging. The first chapter introduces various parameters that affects the bulk electrical resistivity of earth materials and the methodology of measuring DC/IP responses. The second chapter examines the importance of geometry factor and its application in a field experiment. The third chapter presents two dimensional cross-borehole tomography results from two field experiments along with a new color scheme for simultaneous display of resistivity and chargeability tomography. Also, the detectability problem is addressed through numerical modeling. The fourth chapter attempts to construct a three dimensional image of area of interests by combining tomography results from various combinations of surface and borehole tomography measurements. Last but not least, the reports ends with conclusions and outlook/recommendations.

Acknowledgements

I would like to take this opportunity to express my sincere gratitude to my supervisor Prof. Bernd Milkereit for his continuous support and guidance.

My sincere thanks also goes to Prof. Richard Bailey and Dr. Charly Bank for being on my committee and examining my presentation. I would like to thank Prof. Gordon West, Prof. Nigel Edward and Prof. Richard Smith for providing valuable suggestions and Dr. Wei Qian, Dr. Stephane Perrouty for field work support. My thanks also goes to my colleagues and friends Dong Shi, Ramin Saleh, Ken Nurse and Maria Tibbo, Hui Chen, who have supported me in both academic and everyday life.

This project was supported by NSERC, CMIC Footprint and the SUMIT ORF program.

Contents

List of Figures

List of Tables

Table 1: List of Symbols

t	time
σ	conductivity
ρ	resistivity
μ	magnetic permeability
a	electrode spacing
I	current
m	chargeability
U, V	potential
θ	latitudinal angle in spherical coordinate
ϕ	longitudinal angle in spherical coordinate
Φ	cross-correlation coefficient
τ	time lag
R	distance between current and potential electrode
k	geometric factor
r_{sph}	radius of sphere
r_s	distance between the center of the sphere center and current electrode
r	distance between the potential electrode and center of the sphere
R	distance between the current and potential electrode
A, B	current electrode
M, N	potential electrode
$AMNB$	Wenner, Schlumberger array
$AM - BN, AM - NB$	cross-borehole dipole-dipole array
$AM - N, AM - B$	cross-borehole dipole-pole array
P_n^m	associate Legendre function of the first kind
λ	dummy variable of integration
J_0	zeroth order Bessel function of the first kind
α_i, β_i	transmission, reflection coefficient
ϵ	temperature compensation factor

Chapter 1

Introduction

1.1 Background

For near surface earth materials within lithostatic pressure, the bulk electrical resistivity is not only controlled by conductive materials, but also largely influenced by porosity, permittivity, fracturing and fluid content (Ward, 1990). In general, presence of porosity, permittivity and fracturing will increase the bulk electrical resistivity. However, fluid induced into these open spaces may further complicate the situation by further increasing (e.g. oil) or decreasing (e.g. water) the resistivity of the material. Brace et al. 1965 report that the electrical resistivity of water-saturated crystalline rocks generally increases with increasing hydrostatic pressure. From 0 kb to 10 kb, the increase can be as much as three orders of magnitude. For partially saturated rocks, on the other hand, the resistivity decreases with increasing pressure. The resistivity-pressure variation becomes more complicated with the presence of conductive materials. Increase in pressure initially decreases resistivity and then has almost no effect (Brace & Orange, 1968b). Further experiments show that, for water saturated crystalline rock under compressive stress, resistivity first slightly increases until half the fracture stress and then decreases. However, for sandstone under stress, either fully or partially saturated, the resistivity decreases with increasing stress until fracturing occurs (Kate, 1994). Nevertheless, changes in bulk electrical resistivity of earth materials can be used as an indicator of changes in stress and structures.

By Archie's law, porosity and induced fluid have a direct impact on the bulk resistivity (Archie, 1942). Glover et al. 2000; Glover 2010 proposes a modified Archies law by taking both the pore fluid and the hosting rock as conductive phases,

$$\rho_a = \rho_w \phi^{-m} + \rho_s (1 - \phi)^{-p} \tag{1.1}$$

where $p = \frac{log(1-\phi^m)}{log(1-\phi)}$; ρ_s is the resistivity of the host rock; porosity ϕ is fully saturated with fluid of resistivity ρ_w; m is cementation exponent; ρ_a is the resulting bulk resistivity. Figure 1.1 depicts the calculated bulk resistivity of a rock at different porosities as a function of conductivity of the induced pore fluid.

Figure 1.1 shows that even for fluid of low conductivity (10^{-2} S/m - 10^{-1} S/m), saturating porosity of small volume fractions (0.5% - 1.0%), can change bulk resistivity can by up to 10 %. This amount of change sits well above typical instrumental noise level (1 %) and can be well captured by direct current (DC) resistivity imaging. It is also noted that, with pore fluid of higher conductivity (greater than 10
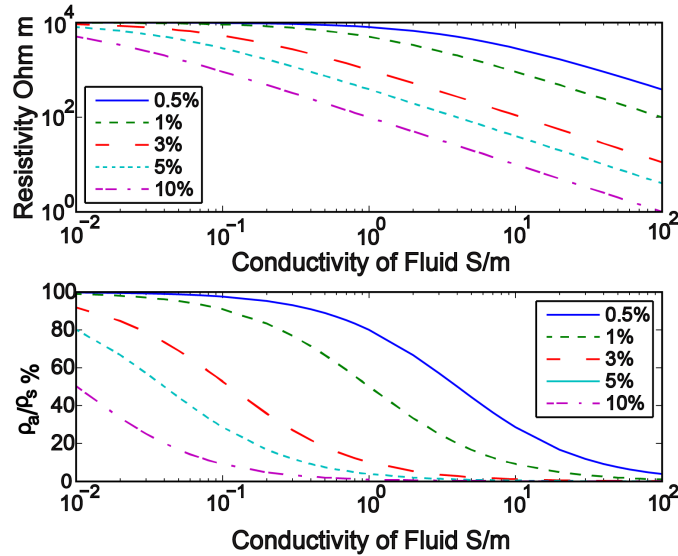
Figure 1.1: The bulk resistivity of a rock as a function of conductivity of induced pore fluid at different porosities ($m = 2$). The numbers in the legend are volume fractions of porosity. The lower end of the conductivity of fluid 10^{-2} S/m corresponds to fresh water and the higher end 10^2 S/m corresponds to brine water. Percentage is $\rho_a/\rho_s \times 100\%$

S/m) and porosity higher than 5%, the bulk resistivity is primarily controlled by the conductivity of the fluid. Under this circumstance, the pore fluid acts as the main conducting phase and the bulk resistivity variation under stress or pressure should be primarily attributed to changes in pore space.

Therefore, in addition to mineral and ground water exploration, DC resistivity method has been demonstrated to be capable to track time lapse changes for geotechnical and environmental monitoring, such as waste leakage, air sparging, steam injection and tracer experiment (Daniels & Dyck, 1984; LaBrecque et al., 1996; Muller et al., 2010; Nimmer et al., 2007; Ramirez et al., 1993; Schima et al., 1996).

The induced polarization (IP) effect was first reported by Conrad Schlumberger in the early 1900s and is usually measured together with DC resistivity measurement (Schlumberger, 1920). When the current injection is being switched on and off, in time domain, it is a phenomenon observed as a voltage delay while in frequency domain as a phase shift (Summer, 1976; Ward, 1990). Although without knowing the nature of the IP effect, it has been demonstrated to be useful in ground water exploration and detecting non-conductive targets, such as disseminated sulphide related gold and copper mineralization (Binley & Kemna, 2005; Seigel, 1971; Hallof et al., 1990; Seigel et al., 2007). The IP effect can be affected by a range of parameters, such as lithology, open spaces and pore fluid chemistry (Binley & Kemna, 2005; Ward, 1990). In addition to mineral exploration, some effort has also been put into investigating its capability in dealing with time lapse monitoring problems (Gallas et al., 2011; Ghorban et al., 2008; Slater & Sandberg, 2000).

Over the last century, surface DC/IP surveys have been well utilized for near surface imaging. Despite their popularity, such surveys are limited by the depth of penetration, especially with the presence of conductive overburden, and repeatability problems (Oldenburg & Li, 1999; Pun & Milkereit, 2011). It has been suggested that, for a target in a homogeneous half-space, one cannot expect to delineate target whose depth is greater than its dimension (Van, 1953; Asfahani, 2005). Also, variation of weather,
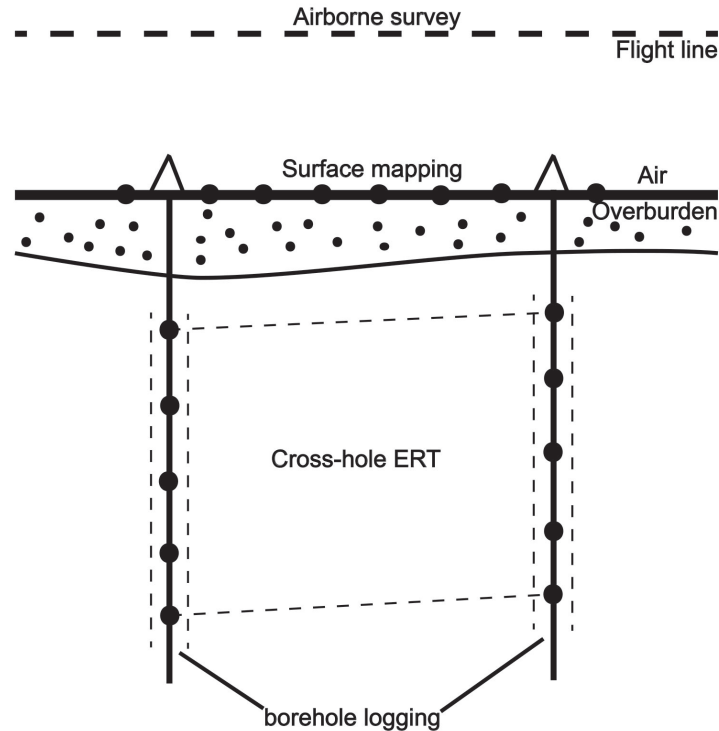
Figure 1.2: Schematic plot of various tools for geophysical investigations

temperature, and water saturation over time can have a strong impact on the electrical properties of near surface materials and thus on surface electrodes. Consequently, measurements over time taken with surface electrodes can have repeatability issues and are thus unreliable for time lapse monitoring. Conventional borehole logging can provide additional, yet limited, information in the immediate vicinity (usually within 30 cm) of the borehole (Asfahani, 2005). It can provide valuable information on targets intersecting the borehole but not on off-hole targets. In recent years, DC/IP surveys conducted in boreholes have become more popular for better depth of investigation, sense of target geometry and good repeatability (Figure 1.2). Pun & Milkereit 2011 shows that the difference between measurements taken in boreholes over hours of time is within 1% of the overall response, which sits as the same level as typical noise. This is largely due to the fact that conditions down a borehole are much more stable than that of on the surface. In addition, with the development of robust inversion schemes, DC/IP taken between boreholes (cross-borehole DC/IP tomography) has become capable to provide more quantitative and rigorous 2D and 3D spatial images between the boreholes (Loke & Barker, 1996b; Zhou & Greenhalgh, 2000; Li & Oldenburg, 2000; Daily et al., 2005). These 2D and 3D images add new capabilities in assisting in geological interpretation than previous curve fitting and pseudo-sections. However, cross-borehole DC/IP tomography surveys generally require additional acquisition time and cost and are limited by borehole availability. Therefore, currently, cross-borehole DC/IP tomography surveys are not as widely practised as surface profile or single-borehole measurements.

1.2 Method

In measuring the bulk resistivity of earth materials, a pair of current electrodes are used to inject current (I) into surrounding materials. The resulting potential difference (ΔV) is measured at a another pair of potential electrodes (Figure 1.3). The current-potential electrode pairs compose an electrode array. For borehole DC/IP surveys, the electrode arrays at different spacings are moved along the borehole(s) for single-borehole and cross-borehole DC/IP measurements.

In this study, the following symbol convention is adopted. The italic letter A denotes the current source ($+I$) and B denotes the current sink ($-I$). M and N denote potential electrodes. For cross-borehole DC/IP tomography, electrodes in different boreholes are separated by dash line $-$. For example electrode array $AM - BN$ represent an array in which electrodes A and M are in the left hand side borehole and A is on top of M; B and N are in the right hand side borehole and B is on top of N (Figure 1.3).

For an electrode planted on the surface of a homogeneous half-space, all injected currents are restricted to flow into the Earth side as the air is non-conductive. For an electrode in a homogeneous full-space, on the other hand, injected currents are free to flow in all directions (Figure 1.4). As a result, the geometry factor, which accounts for the electrode array configuration, for the full-space case is essentially twice the half space case. For resistivity measurements taken in near surface boreholes, we are essentially dealing with a situation between half-space and full-space. For an electrode array $AMNB$ along a near surface borehole (Figure 1.3), electrical images A' and B' are induced with equal current intensity at equal distances to the air-Earth interface above the Earth (Van & Cook, 1966; Telford & Sheriff, 1990). Both electrical images will also results in potentials at M and N. Then the expression for potential difference between M and N is

$$\Delta V = \frac{\rho_a I}{4\pi}(\frac{1}{AM} + \frac{1}{A'M} - \frac{1}{BM} - \frac{1}{B'M} - \frac{1}{AN} - \frac{1}{A'N} + \frac{1}{BN} + \frac{1}{B'N}) \qquad (1.2)$$

The apparent resistivity ρ_a can then be calculated by rearranging Equation 1.2

$$\rho_a = \frac{\Delta V}{I}k, k = 4\pi/(\frac{1}{AM} + \frac{1}{A'M} - \frac{1}{BM} - \frac{1}{B'M} - \frac{1}{AN} - \frac{1}{A'N} + \frac{1}{BN} + \frac{1}{B'N}) \qquad (1.3)$$

where k is the geometry factor for a certain electrode array. The apparent resistivity will approach the true resistivity of the half- or full-space if the dimension of the target is much smaller than the electrode spacing and/or the distance from the target to the electrode array.

Figure 1.5 and 1.6 show time-domain DC/IP data examples with minimal and significant IP effect. When the current is on, a constant voltage response is produced and when the current is switched off, the voltage response instantly goes back to zero. However, some earth materials act as capacitors and the voltage response respond to current variation with a time delay. As shown in Figure 1.6, the voltage gradually increases to its maximum before the injected current is switched off. After the current is switched off, the voltage gradually decays back to zero. The time-domain IP effect can be quantified as chargeability m (Zonge et al., 2005)

$$m = \frac{K}{V_p} \int_{t_1}^{t_2} V_s dt \qquad (1.4)$$

where m is chargeability in mV/V; t_1 and t_2 are time gates between which the voltage is measured;
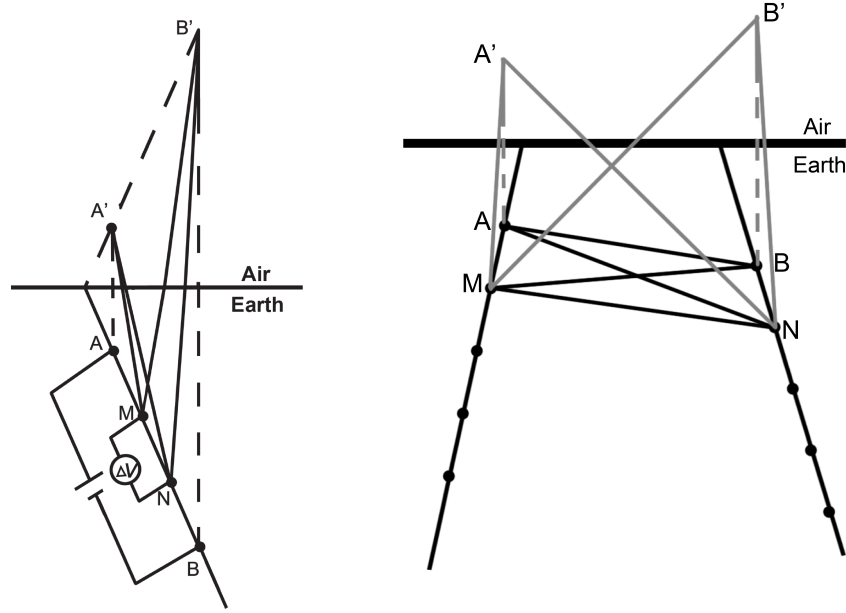
Figure 1.3: (left)Electrode array $AMNB$ along a single-borehole; (right)Dipole-dipole array $AM - BN$ for cross-borehole DC/IP measurement. A' and B' are induced images. Current is injected at electrode A $(+I)$ and sinks at electrode B $(-I)$. Overall potential difference between electrodes M and N $(\Delta V)$is measured

K is normalization constant; V_p is the on-time voltage in Volts (V) and V_s is the decay voltage in mV (Figure 1.7).

The field experiments of this study are conducted with multi-electrode cables and data acquisition system developed by Geoserve in Germany. Positive current is initially switched on for 2048 ms followed by the same amount of off time. Then negative current of the same intensity is switched on and off for the same period of time. The measurement of both injected current and voltage response is taken every 2 ms. For apparent resistivity calculation, ΔV is taken as the average voltage response from 400 ms to 1600 ms after the current is injected. For chargeability calculation, V_p is calculated the same way as ΔV. The time window for decay voltage is taken from 2049 ms (t_1) to 3736 ms (t_2) at every 80 ms for 21 time gates. Then chargeability between each of the 21 time gates is calculated according to Equation 1.4 with $K = 1000$ and the overall chargeability is taken as the average of the last 19 time gates.

Similar to surface DC/IP surveys along profiles, various array types, such as Wenner, Schlumberger, dipole-dipole, can be adopted for single-borehole DC/IP surveys. For DC/IP tomography measurements, multiple acquisition configurations can be adopted, including surface grids, surface-to-borehole and cross-borehole configuration (Bevc & Morrison, 1991; Daniels & Dyck, 1984; Qian et al., 2007; Shima, 1992). For each of the acquisition methods, multiple current-potential electrode arrays, such as pole-pole, pole-dipole, dipole-pole, dipole-dipole, have been studied and adopted (Lytle, 1982; Zhou & Greenhalgh, 1997, 2000). In the field experiment of this study, in order to avoid introducing noise by setting up infinite electrodes, only dipole-dipole arrays are used for tomography measurements. Then the resistance $(\Delta V/I)$ or apparent resistivity (ρ_a) can be calculated and inverted using inversion algorithms to produce a model that best fits the data. In this report, all inversions are carried out in Res2Dinv and Res3Dinv software package using least-squares and smoothness-constrained method(Loke & Barker, 1996a,b).
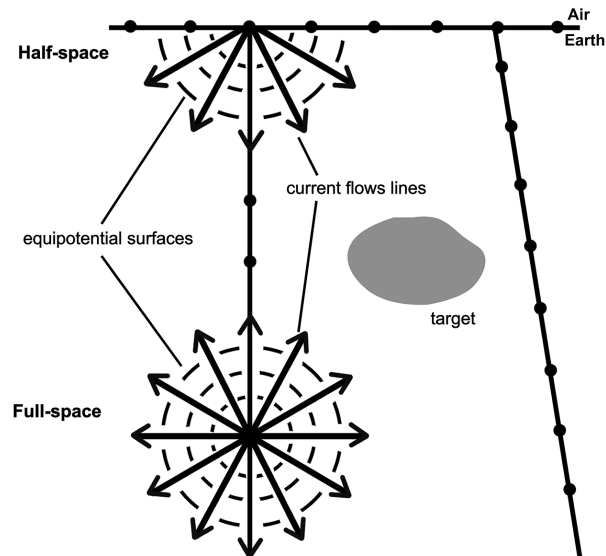
Figure 1.4: Schematic plot of electrode layouts for surface, borehole and surface-to-borehole DC/IP surveys. Black circles represent positions of electrodes
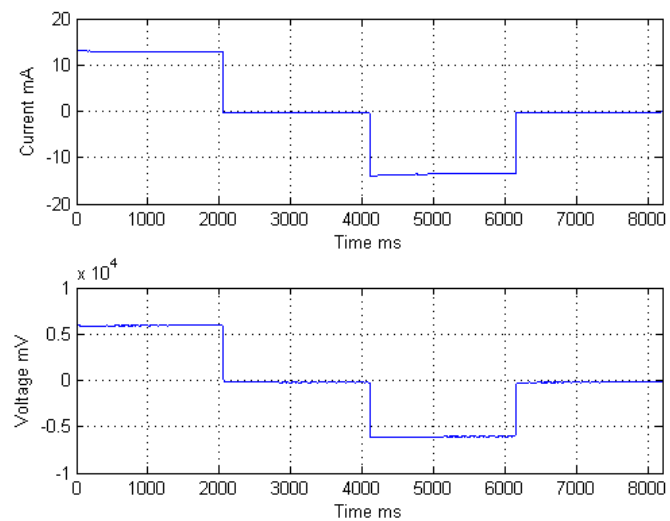
Figure 1.5: Time-domain waveform of DC/IP data example with minimal IP effect; (top) injected current; (bottom) voltage response
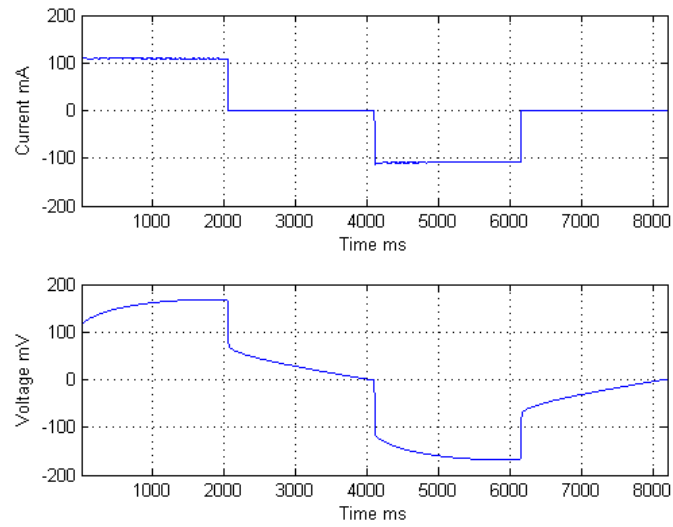
Figure 1.6: Time-domain waveform of DC/IP data example with IP and potentially other distortion effects; (top) injected current; (bottom) voltage response
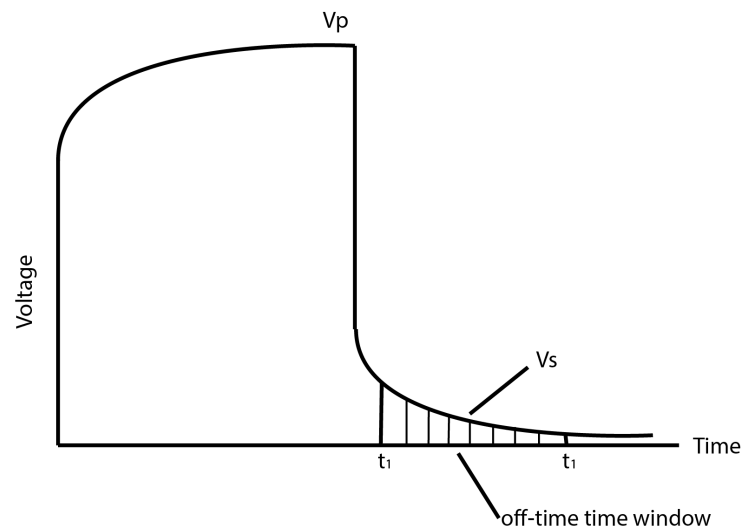
Figure 1.7: Schematic plot of voltage response illustrating chargeability calculation (modified from Zonge et al. 2005)

Chapter 2

Geometrical effect

Although the capability of DC/IP method in dealing with exploration and monitoring problems has been demonstrated, previous studies generally assume the boreholes are drilled near vertically and different boreholes are in the same plane as what is to be imaged. It is also assumed that, regardless of depth from the surface, electrodes in a borehole are in a full-space scenario. However, for practical purposes, boreholes are usually drilled at various dip angles and azimuths in order to maximize geological information to be obtained (Figure 2.1, 2.2). For near-surface borehole DC/IP surveys in particular, we are also dealing with a transition from half-space to full-space. Data processing and inversion without taking such deviation effect can raise errors that are well above typical data noise levels (Oldenborger et al., 2005; Yi et al., 2009). Such errors can be problematic in resolving high resolution structures, especially for time-varying monitoring purposes. This chapter compares the geometry factors of dipping boreholes with geometry factors calculated with full-space or vertical borehole assumptions for the single-borehole and cross-borehole cases. Then a modified geometry factor is proposed to account for both the deviation effect and the water layer for a underwater DC/IP survey.

2.1   Single-borehole

In order to examine the deviation effect, the geometry factor k along a deviated borehole is normalized by the geometry factor in a full-space scenario (k_f)

$$\hat{n}_{kf} = k/k_f \tag{2.1}$$

or in a vertical borehole scenario

$$\hat{n}_{kv} = k/k_v \tag{2.2}$$

Figure 2.3 and 2.4 depict the variation of normalized geometry factors of Wenner array as a function of depth along boreholes dipping at various angles. Both figures show that the normalized geometry factors converge to 1.0. Also, normalized geometry factors along shallow dipping boreholes show more variation than near vertical ones. According to Figure 2.3, the transition from half-space to full-space mostly occurs in the top 20 % of the boreholes, within which boreholes of all dip angles show significant variation. Even for a near vertical borehole dipping at 80 degrees, the total variation can be more than 15 %. In Figure 2.4, it is noted that the transition from deviated to vertical boreholes also mostly occurs
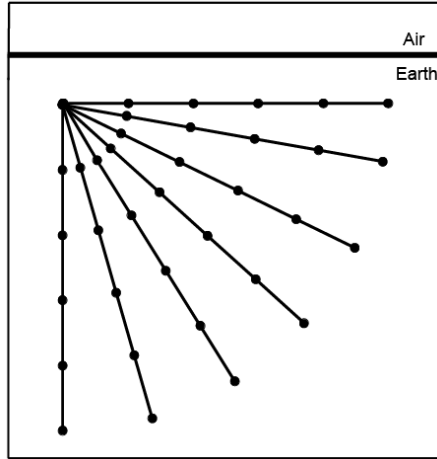
Figure 2.1: Schematic plot of near surface boreholes at different dip angles. Solid black circles denote positions of electrodes
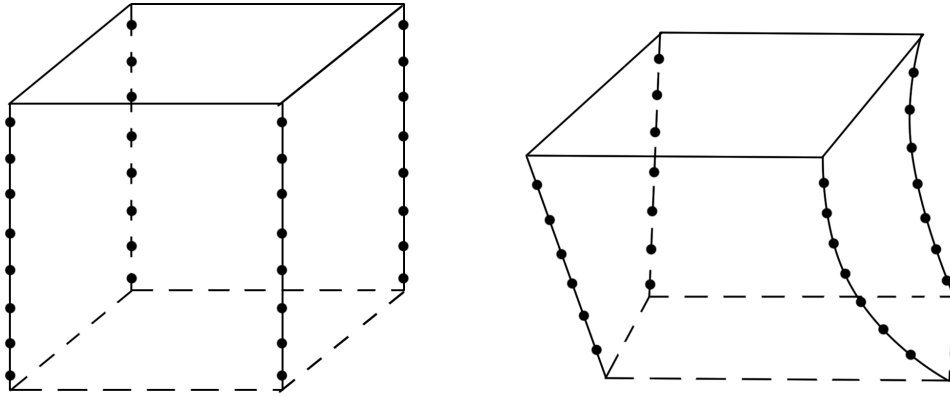
Figure 2.2: Schematic plots of (left) idealized cross-borehole DC/IP tomography survey geometry and (right) actual survey geometry using existing exploration boreholes

within the first 20 % of the boreholes. However, for boreholes with the same dip angles, the deviation and half-space-full-space transition are only significant for shallow dipping boreholes. For a borehole dipping at 60 degrees, the total variation is less than 3 %. For a borehole with a steep dip angle of 80 degrees, the variation is basically within the typical instrumental noise level (1 %). It is also found that, when the first electrode is at depth of 100m, regardless of dip angle, the total variation in both $\hat{n}_{kf}$ and $\hat{n}_{kv}$ becomes less than typical noise level and thus can be neglected. Similar variation pattern is obtained with Schlumberger array.

2.2   Cross-borehole

The normalized geometry factors for cross-borehole array $AM - BN$ are calculated in the same way as the single-borehole case. Electrodes A and M are fixed on the top of the left borehole while B and N are moved from the top to the bottom in the other borehole. The depth of each plot point is calculated
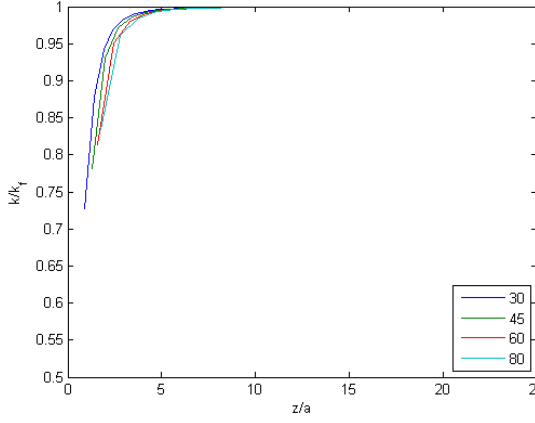
Figure 2.3: Normalized geometry factor $\hat{n}_{kf}$ as a function of depth of Wenner array. Numbers in the legend are dip angles of the boreholes (in degrees). 0.5 corresponds to half-space scenario and 1.0 corresponds to full-space scenario. z is depth
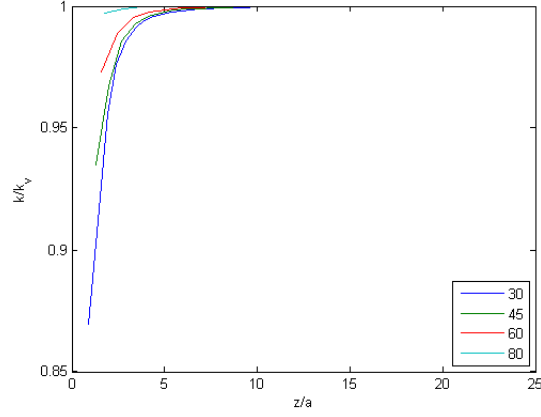
Figure 2.4: Normalized geometry factor $\hat{n}_{kv}$ as a function of depth of Wenner array. Numbers in the legend are dip angles of the boreholes (in degrees). 1.0 corresponds to a vertical borehole scenario

by averaging the depth of the four electrodes. The two boreholes dip at the same angle with opposite azimuths. The results are shown in Figure 2.5 and 2.6.

Similarly as the single-borehole case (Figure 2.3), $\hat{n}_{kf}$ shows a transition from half-space to full-space scenario and most variation occurs within the top 20 % of the borehole (Figure 2.5 and 2.6). However, $\hat{n}_{kf}$ converges to 0.8 instead of 1.0. This suggests that the transition remains significant throughout the borehole and the full-space assumption over simplifies the situation. $\hat{n}_{kv}$ in Figure 2.6 also shows similar behaviour as the single-borehole case with greater overall variation. Even for a steep dipping borehole at 80 degrees, the overall variation, instead of being below noise level, is about 10 % and should be taken into account. When the boreholes separation is smaller than spacing between current and potential electrode in each borehole, a near singular behaviour occurs.

For electrode array $AM - BN$ as depicted in Figure 2.7, the denominator of geometry factor g from Equation 1.3 can be rearranged into

$$g = 2(\frac{1}{a} - \frac{1}{a}\frac{1}{\sqrt{1 + (d/a)^2}} + \frac{1}{a + 2z} - \frac{1}{a + 2z}\frac{1}{\sqrt{(1 + (d/a + 2z)^2}})$$
$$= \frac{2}{a}(1 - \frac{1}{\sqrt{1 + (d/a)^2}}) + \frac{2}{a + 2z}(1 - \frac{1}{\sqrt{1 + (d/a + 2z)^2}})$$

When borehole separation d is smaller than electrode separation a ($d/a + 2z < d/a < 1$),

$$g \sim \frac{2}{a}(1 - (1 - \frac{1}{2}(d/a)^2)) + \frac{2}{a}(1 - (1 - \frac{1}{2}(d/a + 2z))) = \frac{d^2}{a^3} + \frac{d^2}{(a + 2z)^2} \tag{2.3}$$

g becomes considerably small and k becomes a near singular point. Figure 2.9 depicts the variation of $\hat{n}_{kv}$ with depth when borehole separation d is one half of AM ($AM = a$). Because of near singular behaviour of k_v when AM and BN are at the same level, $\hat{n}_{nv}$ behaves non-causally as observed as significant dips in 2.9. Similar behaviour is also seen in Figure 2.8 when the borehole is steeply dipping
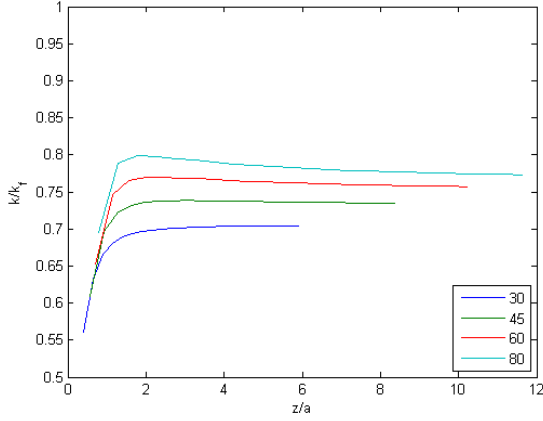
Figure 2.5: Normalized geometry factor $\hat{n}_{kf}$ as a function of depth for cross-borehole array $AM - BN$. Numbers in the legend are dip angles of the boreholes (in degrees). 0.5 corresponds to half-space scenario and 1.0 corresponds to full-space scenario. z is depth. Electrode spacing a is 16m. Two boreholes are separated by 32m on the surface
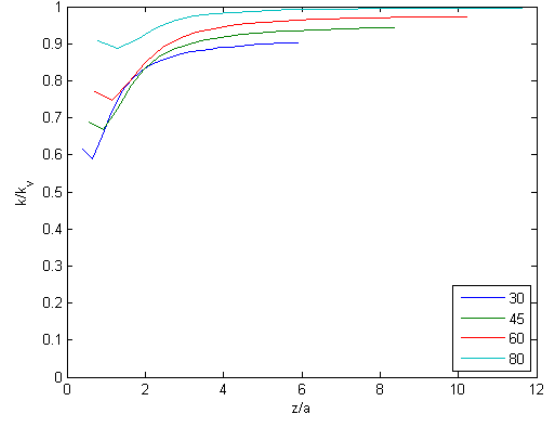
Figure 2.6: Normalized geometry factor $\hat{n}_{fv}$ as a function of depth of for cross-borehole array $AM - BN$. Numbers in the legend are dip angles of the boreholes (in degrees). 1.0 corresponds to a vertical borehole scenario. z is depth. Electrode spacing a is 16m. Two boreholes are separated by 32m on the surface

at 80 degrees. Data acquired at such levels may not be effective signals from potential targets and results in misinterpretation. Such behaviour disappears in boreholes dipping at smaller angles as separation between boreholes becomes greater electrode spacing a. Therefore, it is recommended that extra care should be taken when borehole separation is smaller than electrode spacing. Zhou & Greenhalgh 2000 reports that array $AM - NB$ produces similar inversion results as $AM - BN$ in their synthetic study. As there is no singularity problem in geometry factor in array $AM - NB$, it can be used as an alternative acquisition array when borehole separation is smaller than electrode spacing at certain levels.

On the other hand, for a cross-borehole acquisition geometry as in Figure 2.10, the potential due to $+I$ at A and $-I$ at B at (x, z)

$$V(x, z) = \frac{\rho I}{4\pi} \left(\frac{1}{\sqrt{z^2 + x^2}} - \frac{1}{\sqrt{z^2 + (d - x)^2}} \right) \tag{2.4}$$

Then the horizontal field at distance z below A in the left hand side borehole

$$E(z) = -\frac{\partial V}{\partial x} \mid_{x=0} = \frac{\rho I}{4\pi} \frac{d}{(z^2 + d^2)^{3/2}} \tag{2.5}$$

Differentiating equation 2.2 with respect to borehole separation d,

$$\frac{\partial E(z)}{\partial d} = \frac{\rho I}{4\pi} \frac{(z^2 + d^2)^{3/2} - 3(z^2 + d^2)^{1/2}d^2}{(z^2 + d^2)^3} \tag{2.6}$$

The optimal detecting depth with respect to borehole separation occurs when the above differentiation
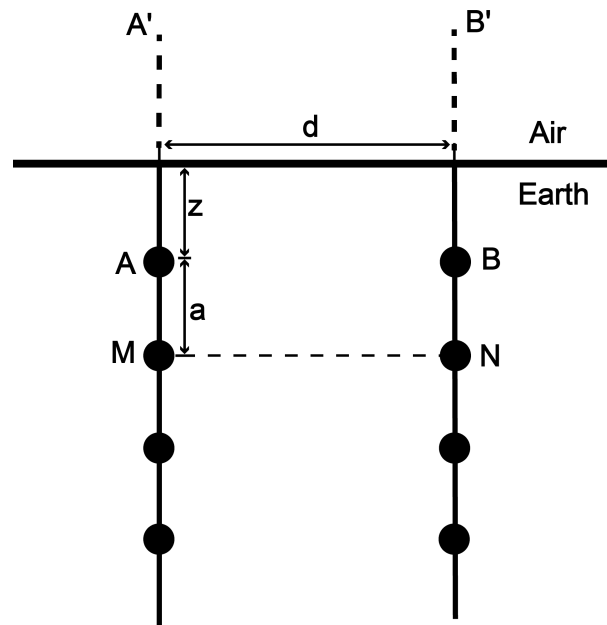
Figure 2.7: Schematic plot of cross-borehole acquisition geometry.
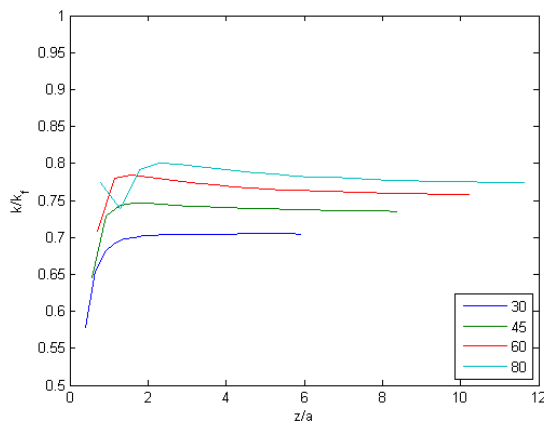
Figure 2.8: Normalized geometry factor $\hat{n}_{kf}$ as a function of depth of for cross-borehole array $AM - BN$. Numbers in the legend are dip angles of the boreholes (in degrees). 1.0 corresponds to a vertical borehole scenario. z is depth. Two boreholes are separated by 8m on the surface
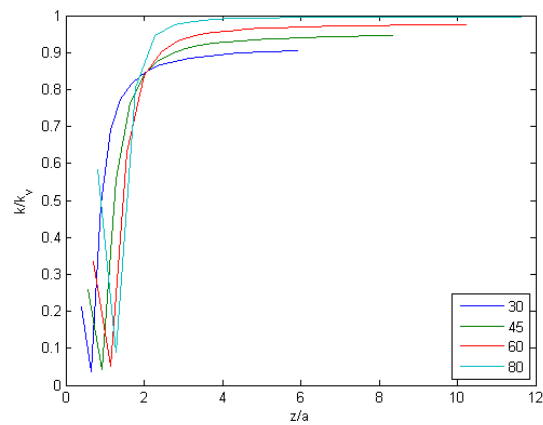
Figure 2.9: Normalized geometry factor $\hat{n}_{kv}$ as a function of depth of for cross-borehole array $AM - BN$. Numbers in the legend are dip angles of the boreholes (in degrees). 1.0 corresponds to a vertical borehole scenario. z is depth. Two boreholes are separated by 8m on the surface
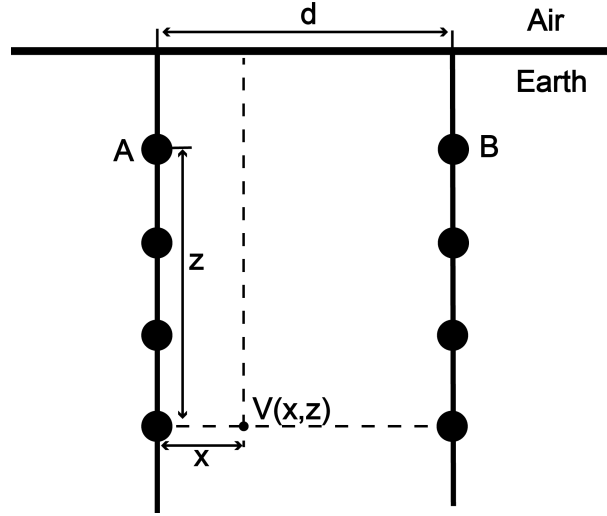
Figure 2.10: Schematic plot of cross-borehole acquisition geometry.

goes to zero

$$\frac{\partial E(z)}{\partial d} = 0 \Rightarrow z = \sqrt{2}d \tag{2.7}$$

and

$$\frac{\partial^2 E(\sqrt{2}d)}{\partial^2 d} < 0 \tag{2.8}$$

Therefore, the maximum horizontal field is reached at $\sqrt{2}$ times the separation of the boreholes below the current electrodes. However, the aforementioned singularity problem may arise with such configuration. Therefore, for boreholes at small separation, the optimal electrode spacing should not be greater than the borehole separation. After each set of measurements, the electrodes can be shifted by a portion of AM to improve resolution and better delineate small scale features.

2.3   Application

A DC/IP monitoring project has been conducted at Ogilvie's lake, Deep River, Ontario. The lake is believed to be closely related to a pristine shallow glaciofluvial groundwater system (Shirokova & Ferris, 2013). Multiple profiles of DC/IP surveys have been conducted both on top and at the bottom of the lake. The lake bottom dips roughly at 10 degrees from the bank to the center of the lake, which is a similar scenario as a shallow dipping borehole. In addition, for the latter case, the electrodes are laid at the interface of lake water and sediments. The injected current, instead of all flowing into homogeneous Earth materials, splits into the water and the Earth. Therefore, the conventional apparent resistivity formula (Equation 1.3) needs to be re-formulated to include the presence of a water layer. This scenario is approximately equivalent to a two layered Earth problem where the electrodes locate at the interface of the first and second layer.

Van & Cook 1966 gives the potential due to a point source in a three layered Earth. Then Daniels 1978 extends the formulation to an n-layered case in a recursion relationship. Assuming the current electrode to be a pole at the origin of cylindrical coordinates, for a point current source in layer 0 of
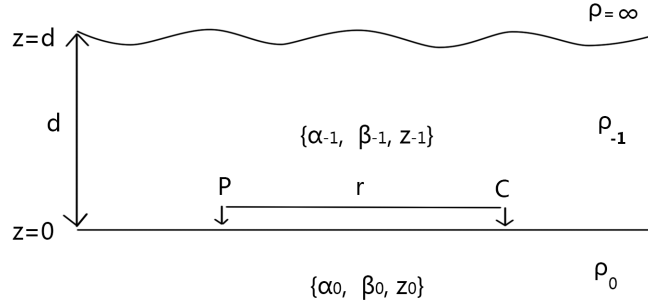
Figure 2.11: The two-layer model. C denotes current electode; P denotes voltage electrode. The thickness of the water is d. All electrodes are on the water-Earth interface.

resistivity ρ_0 (Figure 2.11), the potential measured at P is,

$$U_i(r, z_i) = \frac{I\rho_0}{4\pi} \Big[\int_0^{+\infty} (\alpha_i e^{\lambda z_i} + (\beta_i + 1)e^{-\lambda z_i}) J_0(\lambda r) d\lambda\Big] \tag{2.9}$$

Using the Lipschitz's integral, we get

$$U_i(r, z_i) = \frac{I\rho_0}{4\pi} \Big[\frac{1}{r} + \int_0^{+\infty} (\alpha_i e^{\lambda z_i} + \beta_i e^{-\lambda z_i}) J_0(\lambda r) d\lambda\Big] \tag{2.10}$$

where I is injected current, r is the radial distance between a pair of current electrode and potential electrode; α_i, β_i are transmittance and reflection coefficients in the ith layer; λ is the dummy variable of integration; J_0 is the zeroth order Bessel function of the first kind. The first part of Equation 2.10 is the primary part and is the same as the case where the electrode is in a homogeneous full-space. The second part of the equation is the secondary part due to presence of non-resistive layer above the current electrode. The α term is the part that decays upwards and the β term is the part that decays downwards.

However, Daniels 1978's formulation is unnecessarily complicated by having current and potential electrodes in arbitrary layers and is mainly used for modelling and interpretation. In this study, the scenario can be simplified by replacing all layers above the current electrode by a water layer of thickness d of resistivity rho_{-1} and all layers below the current electrode by a homogeneous half-space of resistivity ρ_0 (Figure 2.11). As the potential electrode is also located at the water-Earth interface, Equation 2.10 can be further simplified by letting $z_i = 0$. Two typos are noted in Daniels's paper and are corrected in the following formulation. The simplified model is depicted in Figure 2.11.

Consequently, Equation 2.10 is simplified to be

$$U_{-1}(r, z_{-1}) = \frac{I\rho_0}{4\pi} \Big[\frac{1}{r} + \int_0^{+\infty} (\alpha_{-1} e^{\lambda z_{-1}} + \beta_{-1} e^{-\lambda z_{-1}}) J_0(\lambda r) d\lambda\Big] \tag{2.11}$$

in the water layer and

$$U_0(r, z_0) = \frac{I\rho_0}{4\pi} \Big[\frac{1}{r} + \int_0^{+\infty} (\alpha_0 e^{\lambda z_0} + \beta_0 e^{-\lambda z_0}) J_0(\lambda r) d\lambda\Big] \tag{2.12}$$

in the Earth layer. $(\alpha_{-1}\ \beta_{-1})$ and $(\alpha_0\ \beta_0)$ are undetermined coefficients to be solved by applying appropriate boundary conditions.

First of all, the current across the air-water interface must be zero as the air is non-conductive. As the current density is proportional to the vertical derivation of potential $(J_z = -\frac{1}{\rho}\frac{\partial U}{\partial z})$, then

$$\frac{\partial U_{-1}}{\partial z}|_{z_{-1}=d} = \frac{I\rho_0}{4\pi}[\int_0^{+\infty}(\lambda\alpha_{-1}e^{\lambda d} - \lambda(\beta_{-1}+1)e^{-\lambda d})J_0(\lambda r)d\lambda] = 0 \qquad (2.13)$$

Setting the integrand to be zero.

$$\alpha_{-1}e^{\lambda d} - (\beta_{-1}+1)e^{-\lambda d} = 0 \Longrightarrow \alpha_{-1} = (\beta_{-1}+1)e^{-2\lambda d} \qquad (2.14)$$

Secondly, the potential at the water-Earth interface must be continuous $U_{-1}|_{z_{-1}=0} = U_0|_{z_0=0}$ so that

$$\alpha_{-1} + \beta_{-1} = \alpha_0 + \beta_0 \qquad (2.15)$$

In addition, the secondary part of the vertical current density should be continuous across the water-Earth interface

$$\frac{1}{\rho_{-1}}\frac{\partial U_{-1}}{\partial z}|_{z_{-1}=0} = \frac{1}{\rho_0}\frac{\partial U_0}{\partial z}|_{z_0=0} \qquad (2.16)$$

Equating the integrands and gets

$$\rho_0\lambda(\alpha_{-1} - \beta_{-1}) = \rho_{-1}\lambda(\alpha_0 - \beta_0) \Longrightarrow \frac{\rho_0}{\rho_{-1}}(\alpha_{-1} - \beta_{-1}) = \alpha_0 - \beta_0 \qquad (2.17)$$

Lastly, U_0 should go to zero as z_0 goes to infinity and go to $\frac{\rho_0 I}{4\pi}$ near the source. Therefore in layer 0

$$\alpha_0 = 0 \qquad (2.18)$$

Solving Equation 2.3 to 2.18 for $(\alpha_{-1}\ \beta_{-1}),(\alpha_0\ \beta_0)$ and get

$$\alpha_{-1} = \frac{e-2\lambda d(\rho_{-1} - \rho_0)}{e-2\lambda d(\rho_{-1} + \rho_0) + (\rho_{-1} - \rho_0)}, \quad \beta_{-1} = -\frac{e-2\lambda d(\rho_{-1} + \rho_0)}{e-2\lambda d(\rho_{-1} + \rho_0) + (\rho_{-1} - \rho_0)} \qquad (2.19)$$

and

$$\alpha_0 = 0, \quad \beta_0 = -\frac{2e-2\lambda d\rho_0}{e-2\lambda d(\rho_{-1} + \rho_0) + (\rho_{-1} - \rho_0)} \qquad (2.20)$$

Then

$$U_0|_{z_0=0} = \frac{I\rho_0}{4\pi}[\frac{1}{r} - 2\frac{\rho_0}{\rho_{-1} + \rho_0}\int_0^{+\infty}\frac{e^{-2\lambda d}}{e^{-2\lambda d} + \frac{\rho_{-1}-\rho_0}{\rho_{-1}+\rho_0}}J_0(\lambda r)d\lambda] \qquad (2.21)$$

Unfortunately, there is not analytical solution to the integral, it has to be calculated numerically.

For a four electrode array $AMNB$, where current is injected at A and sinks at B, potential is measured at M and N, r is replaced with AM, BM, AN and BN:

$$\Delta U = \frac{I\rho_a}{4\pi}(\frac{1}{AM} - \frac{1}{BM} - \frac{1}{AN} + \frac{1}{BN} - $$
$$2\frac{\rho_0}{\rho_{-1} + \rho_0}\int_0^{+\infty}\frac{e^{-2\lambda d}}{e^{-2\lambda d} + \frac{\rho_{-1}-\rho_0}{\rho_{-1}+\rho_0}}[J_0(\lambda AM) - J_0(\lambda BM) - J_0(\lambda AN) + J_0(\lambda BN)]d\lambda$$
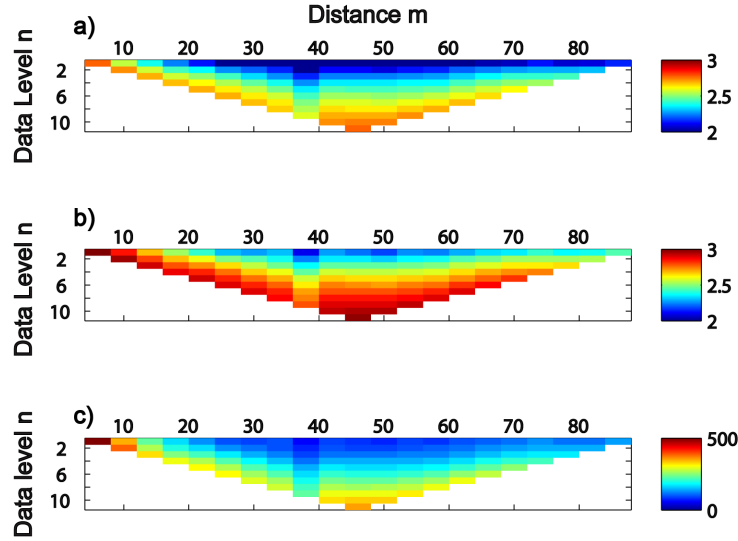
Figure 2.12: Apparent resistivity pseudo-sections at the bottom of the Ogilvie's lake at Deep River in the summer. (*a*) calculated without correction for deviation effect and water layer; (*b*) calculated with corrected geometry factor; (*c*) difference between (*a*) and (*b*). (*a*), (*b*) are in logarithmic scale while (*c*) is in natural number scale.

The apparent resistivity can be calculated by rearranging Equation 2.3

$$
\rho_a = \frac{\Delta U}{I} k_m, \quad k_m = 4\pi/(\frac{1}{AM} - \frac{1}{BM} - \frac{1}{AN} + \frac{1}{BN} -
$$
$$
2\frac{\rho_0}{\rho_{-1} + \rho_0} \int_0^{+\infty} \frac{e^{-2\lambda d}}{e^{-2\lambda d} + \frac{\rho_{-1} - \rho_0}{\rho_{-1} + \rho_0}} [J_0(\lambda AM) - J_0(\lambda BM) - J_0(\lambda AN) + J_0(\lambda BN)] d\lambda
$$

(2.22)

where k_m is the modified geometry factor.

In the lake environment, the resistivity of water is estimated to be $\rho_{-1} = 100 \ \Omega m$ and the resistivity of sediments in contact with the electrodes $\rho_0 = 300 \ \Omega m$. Then k_m can be calculated accordingly. To correct for deviation effect, terms due to electrical images are added to Equation 1.3.

Figure 2.12 compares apparent resistivity pseudo-sections calculated with and without geometry factor corrected for deviation effect and presence of the water layer. Data were acquired using a Schlumberger array at 4m electrode spacing. It clearly shows that, after correction for the water layer, the first few data levels become more resistive and is less affected by the water layer. The difference between (*a*) and (*b*) can be up to 40 % of the apparent resistivity after correction in (*b*). This difference will carry on to inversion and potentially result in misinterpretation.

2.4 Discussion

For near surface borehole DC/IP surveys, the deviation and half-space-full-space transition effects are both depth and dip angle dependent. Especially for shallow dipping boreholes, the vertical borehole and full-space assumptions over simplify the situation. Therefore, in order to accurately image potential

targets, the exact locations of electrode arrays should be obtained so that correct geometry factors can be applied for apparent resistivity calculation. Moreover, for the $AM - BN$ array in cross-borehole measurements, the geometry factor may behave near singularly when the current-potential electrode separation is smaller than the electrode spacing. The singularity problem can be overcome by alternative array $AM - NB$. The imaging capacity of the two types of arrays are compared and discussed in later chapters. The maximum of the horizontal field is reached when the current-potential electrode separation is $\sqrt{2}$ times the borehole separation. Therefore for boreholes at small separation, the current-potential electrode separation should be as large but no greater than the borehole separation.

A modified geometry factor is proposed to account for presence of water layer for under water DC/IP surveys. Application of the modified geometry factor to underwater resistivity data shows that it effectively removes the top low resistivity layer due to presence of a more conductive water layer. In addition, while investigating this time lapse dataset, it is noted that the temperature-resistivity variation of the water layer should also be taken into account for monitoring purposes. By comparing two popular temperature-conductivity relationship of water in the literature, the simple linear temperature-conductivity relationship of water is found to be more effective in temperature correction. Comparison of the two temperature-conductivity relationships are discussed in Appendix A.

Chapter 3

Cross-borehole DC/IP tomography

The concepts of cross-borehole electrical resistivity tomography (ERT) first migrated from medical electrical tomography and are applied in a much larger scale (Daily et al., 2005; Dines & Lytle, 1979; Olayinka & Yaramanci, 2000). Later, inversion scheme for IP tomography become available to assist ERT interpretation without having complete knowledge on the physical controls of IP effect (Cardarelli & Filippo, 2009; Li & Oldenburg, 2000; Kemna et al., 2004). The combination of resistivity and IP tomography provides further constraint in distinguishing different lithology. In this chapter, a 2D color scheme is proposed to display resistivity and chargeability tomography on the same image. Rather than comparing resistivity and chargeability tomography side by side, this new color scheme enables direct visual comparison of the two properties and to assist fast and accurate interpretation. Then single-borehole pseudo-sections and cross-borehole tomography results from two sets of field experiment are presented and are compared. In the end of this chapter, the detectability of cross-borehole measurements is investigated by modeling perturbation due to a spherical anomaly in a homogeneous half-space between boreholes.

3.1 A 2D color scheme for DC/IP tomography display

The 2D color scheme adopts the composition of the three additive color primaries, red, green and blue. The color scheme for resistivity and chargeability, respectively, varies from blue to green and black to red (Figure 3.1). The composition of the two color schemes gives a 2D color scheme with blue, green, purple and yellow at the four corners representing different end members of resistivity-chargeability combinations. Lithology of various resistivity-chargeability combinations can be directly represented by different colors in this color scheme. For example purple indicates a lithology of low resistivity and high chargeability while yellow indicated a lithology of high resistivity and high chargeability.

3.2 Field examples

3.2.1 Surface boreholes, Sudbury North Range

Three surface boreholes, W121, W128 and W130 were available for DC/IP single- and cross-borehole tomography measurements at an exploration site at Sudbury North Range, Ontario. Single-borehole
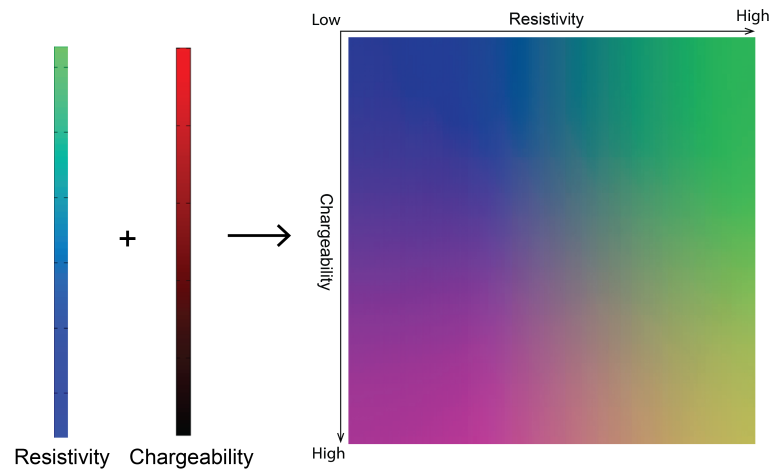
Figure 3.1: 2D color scheme combining resistivity and chargeability data

DC/IP pseudo-sections are shown in Figure 3.2, 3.3 and 3.4 (Schlumberger array). All three boreholes show that the resistivity of the first half of the borehole is more conductive than that of the second half. Near-hole materials are mainly non-chargeable while materials get more chargeable away from the borehole. Relatively conductive while non-chargeable near-hole zones around 100m along the boreholes are likely to be due to the same lithology as the three boreholes are close together near the surface. Also, borehole W121 intersects conductive materials at the end of the borehole. Two small chargeability anomalies along W121 can be observed at 210m and 245m along the borehole, equivalent to depth of 194m and 227m. Two similar anomalies are also observed at 220m and 250m along W128(equivalent to 218m and 249 depth). These two anomalies may be produced by the same chargeable materials intersected by both boreholes.

Cross-borehole DC/IP tomography inversion results are depicted in Figure 3.5. By Figure 3.5, it is shown that all three boreholes intersect a chargeable anomaly at around 200m. Borehole W130 and W121 intersect conductive materials at depth of 175m and below 300m and a chargeability anomaly at around depth of 200m. However, comparing with single-borehole pseudo-sections, it is suggested that these anomalies are actually off-hole rather than intersected by the boreholes except for the resistivity anomaly at the end of W121. Borehole W128 mainly goes through resistive materials while the chargebility anomaly it intersects at depth of 230m may be related to the anomaly the other two boreholes intersect at similar depth. Therefore, although cross-borehole tomography is a powerful tool in providing spatial image of resistivity and chargeability distributions, single-borehole data should also be collected to assist accurate interpretation.

The resistivity and chargeability distribution each provides ample information for interpretation. However, it is difficult to know how and how much the the two parameters are related in the surveyed area by visual inspection with commonly used RGB color scheme. Figure 3.6 shows similar information as in Figure 3.5. However, when the two figures in Figure 3.6 are combined and gives Figure 3.7, the relation and degree of relation between the resistivity and chargeability anomalies can be clearly identified and inferred by the hue and saturation of color in the color scheme. 3.7 unveils that the major chargeability anomaly at depth around 200m is associate with both conductive and resistive materials, observed as color variation from purple to yellow and green. This can be caused by different lithology or change in electrical properties within the same lithology. The economic value of potential targets can

Figure 3.2: (Apparent resistivity (left) and chargeability (right) pseudo-section along borehole W121 (Schlumberger array). Resistivity is in $log_{10}(\Omega m)$. Chargeability is in mV/V. Electrode spacing is 4m

Figure 3.3: Apparent resistivity (left) and chargeability (right) pseudo-sections along borehole W128 (Schlumberger array). Resistivity is in $log_{10}(\Omega m)$. Chargeability is in mV/V. Electrode spacing is 8m

be then be assessed accordingly.

At this exploration site, most of the resistive rocks the boreholes intersect are norite in the hanging wall section of the Sudbury basin. The end of boreholes may reach the hanging wall/foot wall contact and intersect contact mineralizations as suggested by the apparent resistivity pseudo-section of W121.

3.2.2 Boreholes in a deep mine, Sudbury East Range

Four boreholes in a deep mine at Sudbury East Range, Ontario, were available for DC/IP measurements on the 1300 and 1700 level. In borehole NRS130075 and NRS170143, only single-borehole DC/IP measurements were conducted in collaboration with borehole logging group from the University of Alberta. In NRS170143 and NRS170100, both single- and cross-borehole DC/IP data were collected. The purpose of this survey is both for exploration and to establish a baseline for time lapse monitoring of potential stress and structural changes as mining operations progress.

Borehole NRS130075 intersects a relatively conductive zone at 50m along the borehole and the rest of near-hole materials remains resistive (Figure 3.8). However, off-hole materials get more conductive away from the borehole. The overall chargeability response in NRS130075 except for two small anomalies at 250m and 290m along the borehole. The resistivity response in borehole NRS170143 varies by over
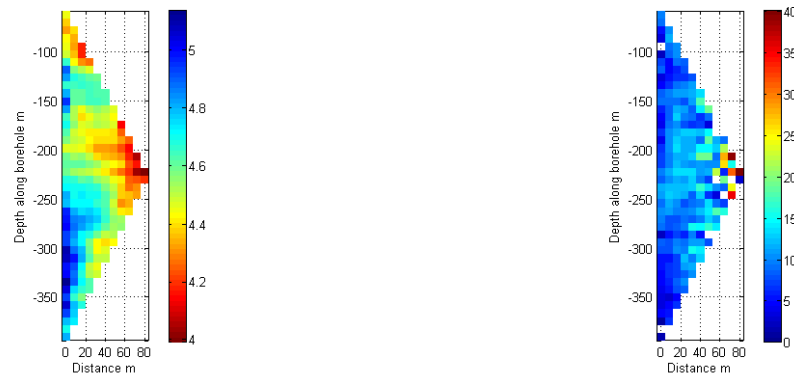
Figure 3.4: Apparent resistivity (left) and chargeability (right) pseudo-sections along borehole W130 (Schlumberger array). Resistivity is in $log_{10}(\Omega m)$. Chargeability is in mV/V. Electrode spacing is 8m
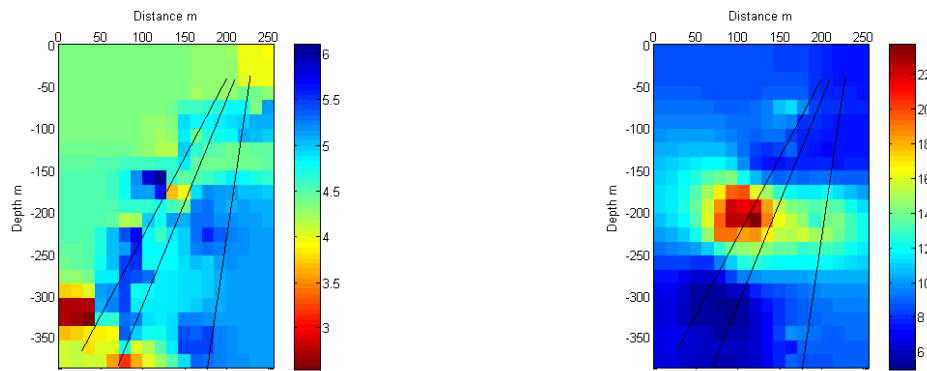
Figure 3.5: (left) Resistivity tomography inversion result; (right) chargeability tomography inversion result in commonly used RGB color scheme. Resistivity is in $log_{10}(\Omega m)$ and chargeability is in natural number scale (mV/V). The horizontal axis is distance on the surface in meters. Black solid lines represent positions of boreholes where the measurements were taken. Borehole numbers from left to right are W130, W121 and W128
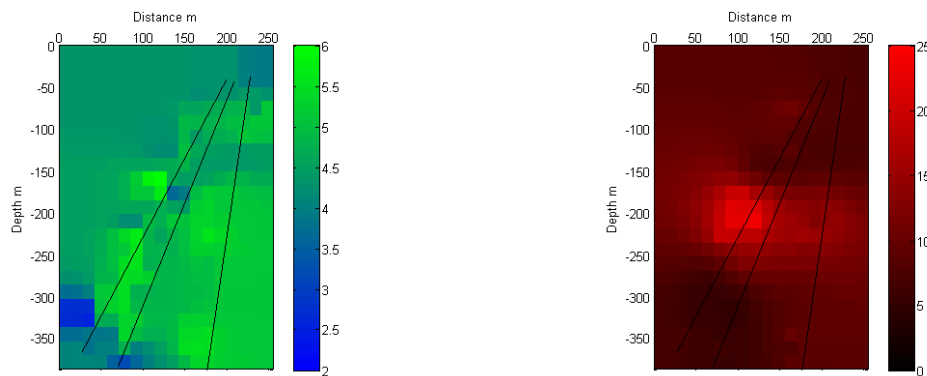
Figure 3.6: Resistivity tomography in blue to green color scheme and chargeability tomography in black to red color scheme
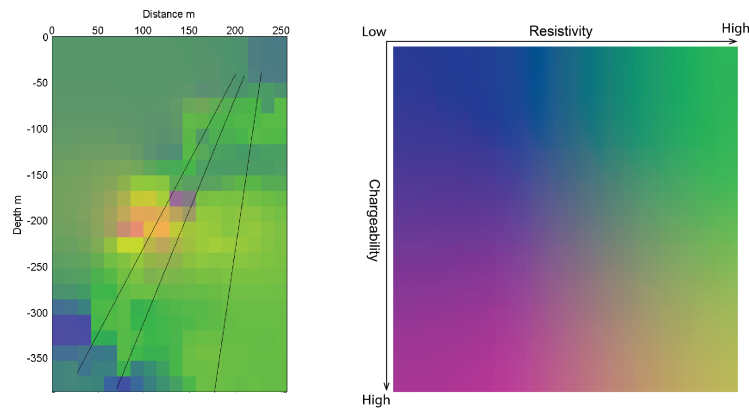
Figure 3.7: Combined resistivity and chargeability result in the new 2D color scheme. Resistivity is in $log_{10}(\Omega m)$ and chargeability is in mV/V

Figure 3.8: Apparent resistivity (left) and chargeability (right) pseudo-sections along borehole NRS130075 (Schlumberger array). Resistivity is in $log_{10}(\Omega m)$. Chargeability is in mV/V. Electrode spacing is 4m

three orders of magnitude with two in-hole conductive anomalies at 160m and from 250m to 290m along the borehole. These two conductive anomalies roughly coincide with chargeability anomalies while the chargeability anomaly from 250m to 290m along the borehole appears slightly off-hole.

Figure 3.10 (NRS170100) recovers both in-hole and off-hole resistivity and chargeability anomalies at various resistivity-chargeability combinations while NRS170162 (Figure 3.11) mainly intersect a low resistivity and high chargeability anomaly which extends away from the borehole. Tomography results recovers similar anomalies (Figure 3.12). However, it is noted that these anomalies are associated with individual boreholes rather than connected across the two boreholes. The middle area has small variation in both resistivity and chargeability, suggesting a relatively uniform lithology, which potentially can be changed with mining operations. It is also suspected that as the borehole separation (more than 100m) greatly exceeds current-potential electrode spacing in each borehole (16m), the resolution between boreholes can be too poor to recover detailed features, especially for the second half where the boreholes are further separated. The resistivity and chargeability variation may not be as uniform as suggested in the current tomography result. As all boreholes have significant in-hole or off-hole chargeability

Figure 3.9: Apparent resistivity (left) and chargeability (right) pseudo-sections along borehole NRS170143 (Schlumberger array). Resistivity is in $log_{10}(\Omega m)$. Chargeability is in mV/V. Electrode spacing is 8m

Figure 3.10: Apparent resistivity (left) and chargeability (right) pseudo-sections along borehole NRS170100 (Schlumberger array). Resistivity is in $log_{10}(\Omega m)$. Chargeability is in mV/V. Electrode spacing is 16m

anomalies, chargeability may be used as another parameter in addition to originally proposed resistivity monitoring only.

Boreholes at this experiment site experience a transition from the hanging wall to the foot wall of the Sudbury Basin. The anomalies detected by the DC/IP surveys may be either due to mineralization at the hanging wall-foot wall contact or in the Sudbury breccias of the foot wall section.

3.3 Detectability: modeling study on a spherical anomaly between boreholes

Since the 1930s, the response of a conductive sphere obtained with various surface and buried DC resistivity arrays has been extensively studied (Daniels, 1977; Merkel & Alexander, 1971; Van, 1953; Telford & Sheriff, 1990; Webb, 1931). Due to symmetry of a sphere, modeling a spherical anomaly is usually much simpler and faster than modeling other shaped bodies using finite-difference or finite-element methods, while providing instructive information. Lytle 1982 compares the apparent resistivity

Figure 3.11: Apparent resistivity (left) and chargeability (right) pseudo-sections along borehole NRS170162 (Schlumberger array). Resistivity is in $log_{10}(\Omega m)$. Chargeability is in mV/V. Electrode spacing is 16m
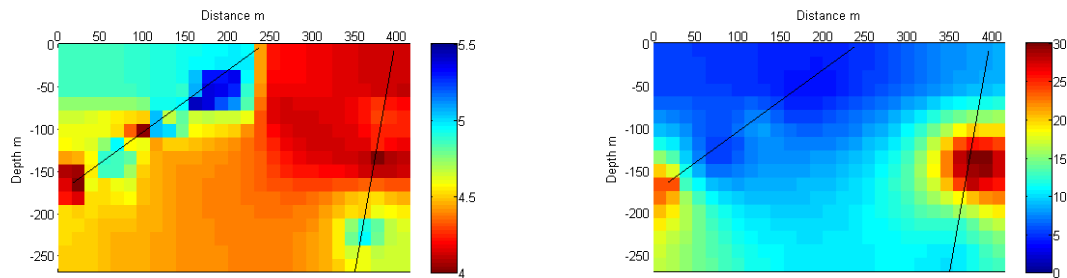
Figure 3.12: (left) Resistivity tomography inversion result; (right) chargeability inversion result in commonly used RGB color scheme. Resistivity is in $log_{10}(\Omega m)$ and chargeability is in mV/V. The horizontal axis is distance in the tunnel in meters. Black solid lines represent positions of boreholes where the measurements were taken. Borehole numbers from left to right are NRS170143 and NRS170100
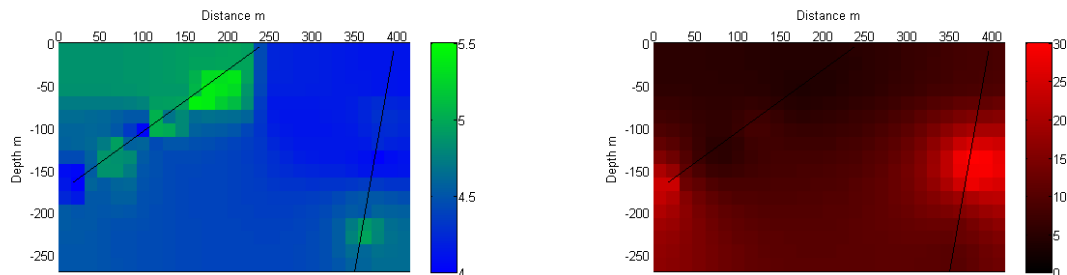
Figure 3.13: Resistivity tomography in blue to green color scheme and chargeability tomography in black to red color scheme between NRS170143 and NRS170100
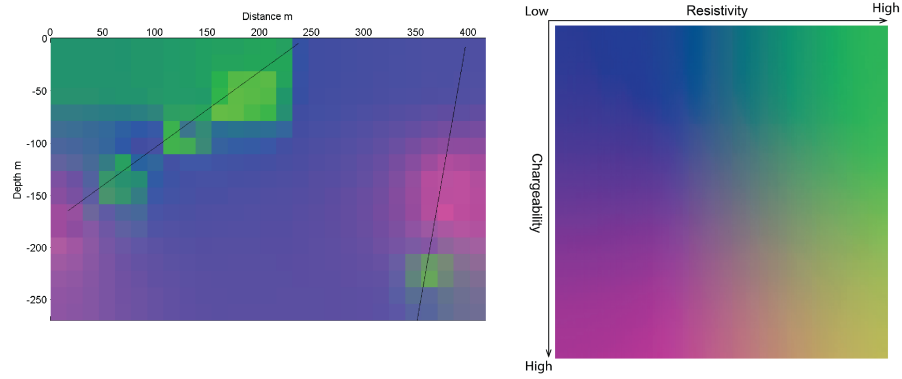
Figure 3.14: Combined resistivity and chargeability tomography result in the new 2D color scheme between NRS170143 and NRS170100. Resistivity is in $log_{10}(\Omega m)$ and chargeability is in mV/V

perturbation due to a conductive sphere for single- and cross-borehole surveying using a pole-pole array. It is suggested that cross-borehole probing provides azimuth information as well as greater detectability than single-borehole. However, the detectability of more complicated three- and four- electrode arrays remains to be investigated.

This section first presents the mathematical formulas of voltage response of a sphere anomaly embedded in a homogeneous half-space due to low frequency injected current based on Budak et al. 1964 and Lytle 1982. The half-space and sphere can be of arbitrary resistivity. Then modelling results with pole-dipole and dipole-dipole arrays are compared and discussed.

In the case of low frequency direct current, the electrical field $\mathbf{E}$ is the gradient of potential V

$$\mathbf{E} = -\nabla V \tag{3.1}$$

By Ohm's law,

$$\mathbf{J} = \sigma \mathbf{E} \tag{3.2}$$

where σ is conductivity of the medium. Therefore,

$$\mathbf{J} = -\sigma \nabla V \tag{3.3}$$

For a conserved charge within a volume τ enclosed by surface S,

$$\int_S \mathbf{J} d\mathbf{a} = 0 \tag{3.4}$$

Then by Green's theorem

$$\int_S \mathbf{J} d\mathbf{a} = \int_V \nabla \mathbf{J} d\tau \tag{3.5}$$

and at the point of this charge

$$\nabla \mathbf{J} = -\nabla \nabla (\sigma V) = -(\nabla \sigma \nabla V + \sigma \nabla^2 V) = 0 \tag{3.6}$$
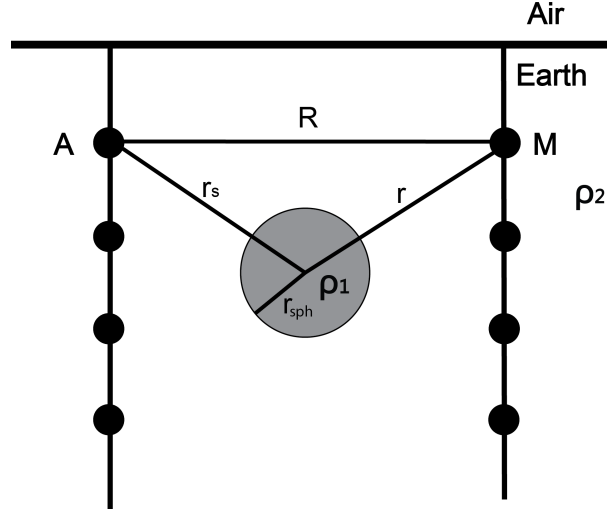
Figure 3.15: Schematic plot of a sphere anomaly of radius r_{sph}, resistivity ρ_1 located between two boreholes in a homogeneous half-space of resistivity ρ_2 (adopted from Lytle., 1982). The center of the sphere is the origin of the spherical coordinate system

As a result, we get the Laplace's Equation

$$\nabla^2 V = 0 \tag{3.7}$$

Morse and Feshbach (1953) gives the general solution for V in spherical coordinates

$$V(r, \theta, \phi) = \sum_{n=0}^{\infty} \sum_{m=0}^{n} (A_{mn} r^n + B_{mn} r^{-n-1}) P_n^m(cos\theta) cos m\phi \tag{3.8}$$

where A_{mn}, B_{mn} are coefficients to be determined from boundary conditions and governs potential inside and outside the sphere respectively. $P_n^m(cos\theta)$ is the associate Legendre function. Then for current source I located outside or at the edge of the sphere ($r_s > r_{sph}$), the resultant potential measured at r from the center of the sphere in spherical coordinate system (Figure 3.15)

$$V = \frac{I\rho_2}{4\pi R} + \sum_{n=1}^{\infty} \frac{I r_{sph} \rho_2}{4\pi r_s r} \frac{\rho_1 - \rho_2}{(n+1)\rho_1 + n\rho_2} n \left(\frac{r_{sph}^2}{r_s r}\right)^n P_n(cos\gamma) \tag{3.9}$$

and for $r \leq r_{sph}$

$$V = \frac{I\rho_2}{4\pi r_s} + \sum_{n=1}^{\infty} \frac{I r^n \rho_1 \rho_2}{4\pi r_s^{n+1}} \frac{2n+1}{(n+1)\rho_1 + n\rho_2} P_n(cos\gamma) \tag{3.10}$$

where $cos\gamma = cos\theta cos\theta_s + sin\theta sin\theta_s cos(\phi - \phi_s)$. If the current source is inside the sphere, the resultant potential measured inside the sphere ($r < a$) is calculated to be

$$V = \frac{I\rho_1}{4\pi R} + \sum_{n=0}^{\infty} \frac{I\rho_1}{4\pi r_{sph}} \left(\frac{r_s r}{r_{sph}^2}\right)^n (\rho_1 - \rho_2) \frac{n+1}{(n+1)\rho_1 + n\rho_2} P_n(cos\gamma) \tag{3.11}$$
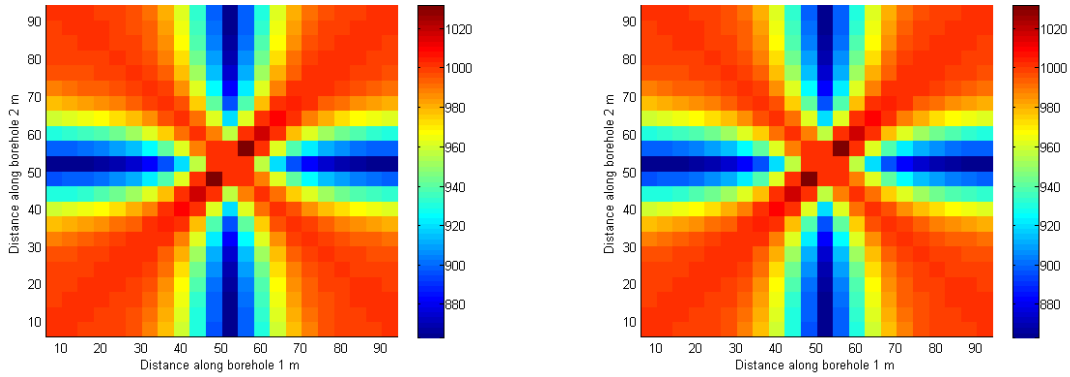
Figure 3.16: Apparent resistivity of the sphere model with dipole-dipole array $AM - BN$ (left) and $AM - NB$ (right)

and the potential measured outside the sphere ($r \geq r_{sph}$)

$$V = \sum_{n=0}^{\infty} \frac{I\rho_1\rho_2}{4\pi r}(\frac{r_s}{r})^n \frac{2n+1}{(n+1)\rho_1 + n\rho_2} P_n(cos\gamma) \tag{3.12}$$

For a multi-electrode arrays, the resulting potentials can be calculated by superposition of voltage responses due to different current electrodes. Figure 3.16 depicts the apparent resistivity perturbation due to a conductive sphere detected by different dipole-dipole cross-borehole arrays. Electrodes in each borehole are laid from 0 to 100m at 4m spacing. The two boreholes are separated by 40m and the sphere is placed in the middle of the boreholes at 50m. The radius of the sphere is 16m and the resistivity contrast (ρ_2/ρ_1) between the sphere and the homogeneous half-space is 100 (Figure 3.15). Although different in acquisition geometry, the two different arrays give identical apparent resistivity response as confirmed by Figure 3.17. Similarly, different pole-dipole arrays gives identical response with the sphere model (Figure 3.18). Comparing responses from dipole-dipole and pole-dipole arrays, it is found that pole-dipole array gives greater perturbation under the same modelling parameters(Figure 3.19). The same conclusion can be reached by setting the sphere at different depths. Therefore, pole-dipole array offers greater detectability and can be a more powerful tool in detecting small perturbation such as in tracer experiments.

Figure 3.20 depicts the total variation in apparent resistivity due to the spherical anomaly as a function of borehole separation (d) and resistivity contrast between the sphere and the homogeneous half-space. Compared with resistivity contrast, the borehole separation with respect to the dimension of the sphere has a much greater impact on the detectability of the anomaly. It is found that, regardless of resistivity contrast, the borehole separation should not exceed two times the diameter of the sphere in order for a detectable perturbation to be detected.

3.4   Discussion

Compared with pseudo-sections from single-borehole surveys, cross-borehole DC/IP tomography provides directional constrained spatial image of resistivity and chargeability distribution between boreholes and enables more rigorous and quantitative interpretation. However, as observed in the previous field ex-
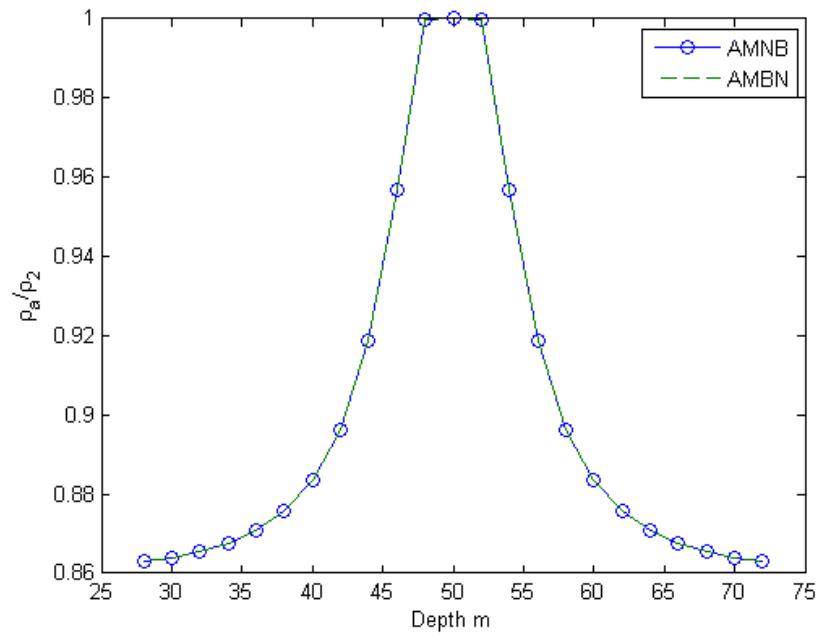
Figure 3.17: Apparent resistivity perturbation due a conductive sphere between borehole with dipole-dipole array $AM - BN$ and $AM - NB$. AM is fixed at 50m at borehole 1 while BN or NB is shifted along the other borehole
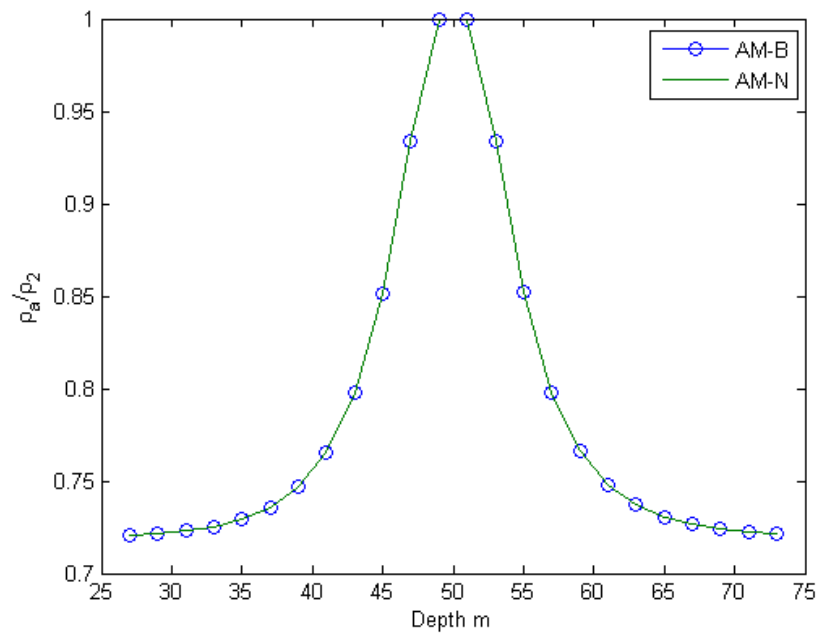
Figure 3.18: Apparent resistivity perturbation due a conductive sphere between borehole with pole-dipole array $AM - B$ and $AM - N$. AM is fixed at 50m at borehole 1 while B or N is shifted along the other borehole
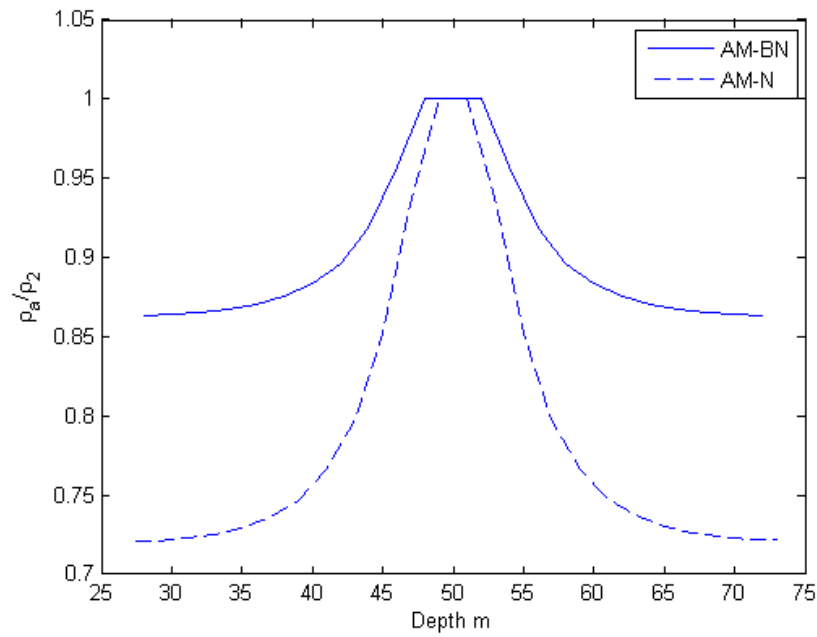
Figure 3.19: Comparison of apparent resistivity along the borehole acquired with dipole-pole $AM-N$ and dipole-dipole $AM-BN$ array
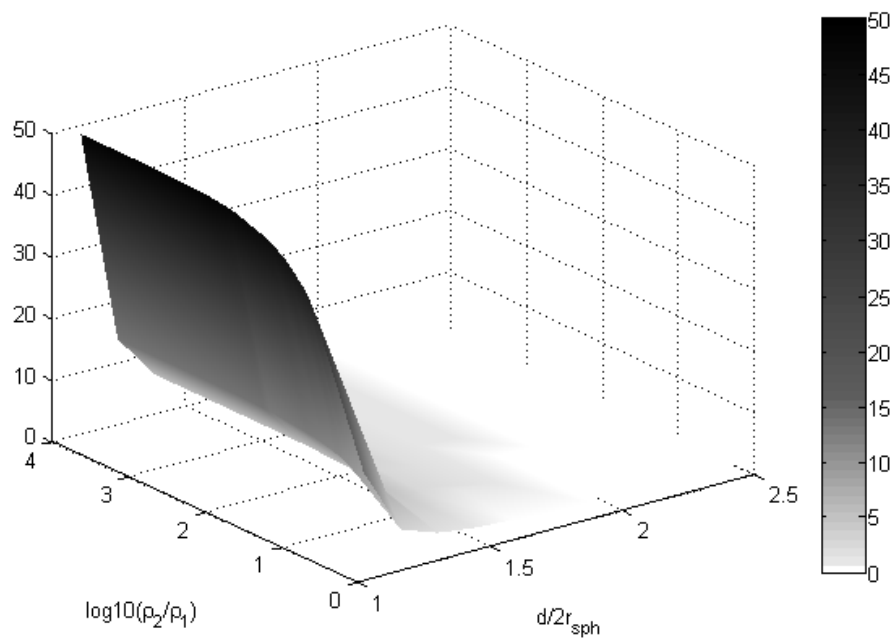
Figure 3.20: Percentage of variation in apparent resistivity due a spherical anomaly between boreholes at various borehole separations and resistivity contrasts

ample at Sudbury North Range, the tomography can also be strongly affected by anomalies that are not in the plane as what is to be imaged. Therefore, it is necessary to compare cross-borehole tomography results with single-borehole pseudo-sections for accurate interpretation.

A 2D color scheme is proposed and it enables simultaneous display of the resistivity and chargeability data on the same image. With the aid of this color scheme, various combinations of resistivity-chargeability variation can be directly visualized and be used to further differentiate different lithology. This color scheme can also be applied to display other combinations of geophysical data, such as V_p and V_s, NMR and porosity, stress and V_p. In addition to better characterize different lithology, it can also be used to show the correlation between two parameters.

Apparent resistivity perturbation due to an off-hole spherical anomaly captured by various three- and four-electrode cross-borehole arrays are calculated and compared. Modelling results show that dipole-dipole arrays $AM - BN$ and $AM - NB$ give identical response, so do pole-dipole arrays $AM - B$ and $AM - N$. Almost identical tomography results are also obtained with $AM - BN$ and $AM - NB$ arrays in a field experiment at Canadian Malartic Mine (Chapter 4). Moreover, for the same anomaly, pole-dipole arrays generally capture greater perturbation than dipole-dipole arrays. Thus, in field experiment, pole-dipole arrays offer better signal strength and are more recommended for geotechnical and environmental monitoring surveys where there is little noise for the infinite electrode. In addition, it is found that the detectability of cross-borehole measurements is primarily determined by borehole separation rather than resistivity contrast. In order to get effective response from the target in the middle of the boreholes, the borehole separation should not be more than two times greater than the dimension of the target.

Chapter 4

Towards 3D

As geological features are three dimensional, potential targets can only be fully recovered by 3D DC/IP surveys. Conventional 3D DC/IP surveys adopt a layout of square or rectangular electrode grid on the surface and measurements are taken at various current-potential electrode combinations (Loke, 2001). However, such 3D surveys have not become commonly practice for either exploration or monitoring as they require a large number of electrodes and measurements and therefore are not economic nor time efficient. In addition, similar to 2D surface DC/IP surveys, the data resolution decreases exponentially with depth (Oldenburg & Li, 1999). However, with the availability of boreholes, surface-to-borehole and cross-borehole measurements can be taken in addition to surface measurements. This can potentially greatly reduce the number of electrodes required on the surface while providing depth constrained tomography results. A combination of cross-borehole, surface-to-surface, surface-to-borehole DC/IP surveys were conducted at an exploration site of Canadian Malartic Mine. Three boreholes and three surface lines were used and measurements were taken at various cross-borehole, surface-to-borehole and surface-to-surface combinations (Figure 4.1). The three boreholes are approximately 100m apart with similar dip and azimuth. The three surface lines start from the borehole collars and run at similar azimuths as the boreholes. Previous surface mapping and geophysicald surveys have identified gold deposits and near surface IP anomalies. The goal of this field experiment is to better delineate the distribution of gold deposits at depth and to investigate the 3D DC/IP imaging capability with combinations of proposed acquisition geometry. Unless specified, tomography data were acquired with dipole-dipole array $AM - BN$. One of the cross-borehole surveys was also conducted with another dipole-dipole array $AM - NB$ to compare the detectability of the two arrays.

4.1   Single surface lines

The three surface lines are all 124m in length using 4m electrode spacing. The measurements were taken with Schlumberger array and the apparent resistivity and chargeability pseudo-sections are shown from Figure 4.2 to 4.4. Figure 4.5 gives waveforms examples of injection current and voltage response with and without IP or other distortion effects measured in L3 survey. Pseudo-sections of L1 and L2 show similar resistivity and chargeability patterns. Two vertical bands of low resistivity anomalies occur in the first half of the lines, in which the location of the first band in L2 coincides with an outcrop containing low grade gold mineralization. The chargeability increases with increasing current-potential
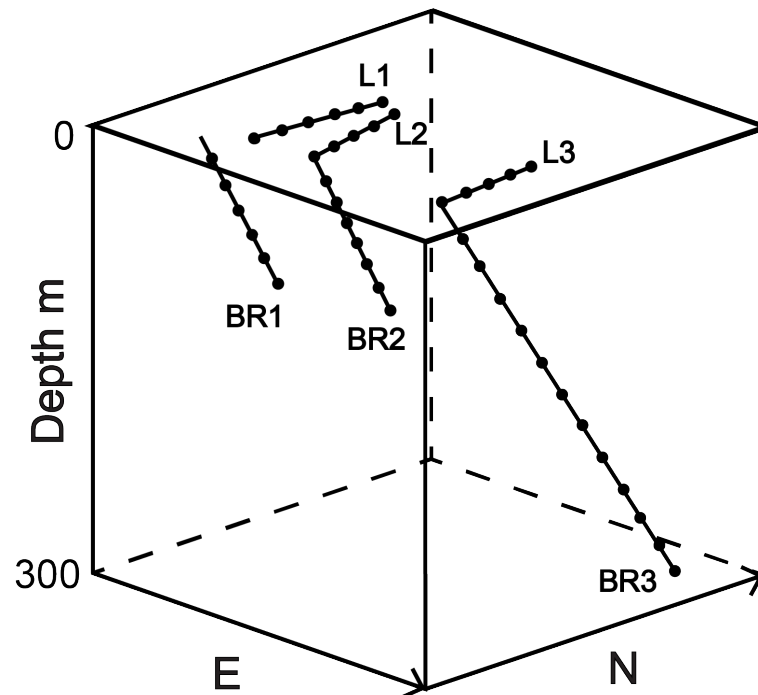
Figure 4.1: 3D DC/IP survey acquisition geometry at an exploration site of Canadian Malartic Mine. BR stands for borehole and L stands for line

electrode separation (depth). Similar chargeability distribution is observed in L3 and it is expected that similar apparent resistivity distribution will be observed. However, the apparent resistivity at similar position is consistently negative. In the vertical negative apparent resistivity zone, the polarity of voltage response is reversed with respect to the injection current. Figure 4.6 shows a waveform example of such phenomenon. When $+I$ is injected at A, instead of regularly getting positive voltage response as in Figure 4.5, negative voltage response is measured. Such reversed voltage response is measured again when the polarity of the injected current is reversed. It is also noted that the voltage firstly increases to maximum and then decreases during current-on time. Similar voltage decay pattern is also measured around the voltage reversal zone (Figure 4.7). These non-causal response are obtained in a systematic manner and the location of the voltage reversal zone coincides with one of gold mineralization zones that has been mapped by the geologist with gold content up to greater than 1 ppm. Therefore, they can be strongly associated with the gold mineralization system instead of instrumental errors. Such responses have not been found to be reported in the literature and the exact physical causes remain to be investigated. A few speculated earth models tentatively to explain such responses, together with the use of cross-correlation coefficient to map such responses, are proposed and discussed in Appendix C.

4.2 Single-boreholes

The apparent resistivity and chargeability pseudo-sections are shown from Figure 4.8 to 4.10. Pseudo-sections of BR1 and BR2 both show relatively small resistivity contrast (within one order of magnitude) and similar chargeability variation (within 25 mV/V). The apparent resistivity pseudo-sections of BR3 shows greater variation and the first half of the borehole is generally more conductive than the second

Figure 4.2: Apparent resistivity (left) and chargeability (right) pseudo-section of L1 (Schlumberger array). Resistivity is in $log_{10}(\Omega m)$. Chargeability is in mV/V. Electrode spacing is 4m
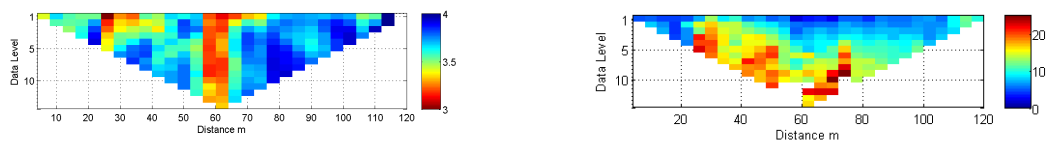
Figure 4.3: Apparent resistivity (left) and chargeability (right) pseudo-section of L2 (Schlumberger array). Resistivity is in $log_{10}(\Omega m)$. Chargeability is in mV/V. Electrode spacing is 4m
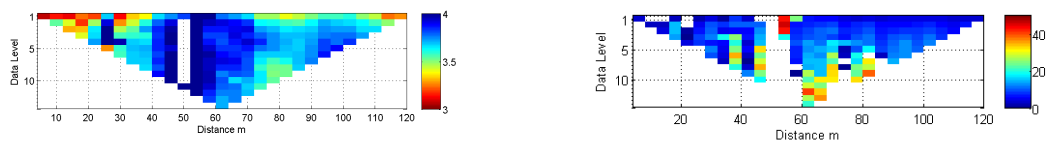
Figure 4.4: Apparent resistivity (left) and chargeability (right) pseudo-section of L3 (Schlumberger array). Resistivity is in $log_{10}(\Omega m)$. Chargeability is in mV/V. Electrode spacing is 4m
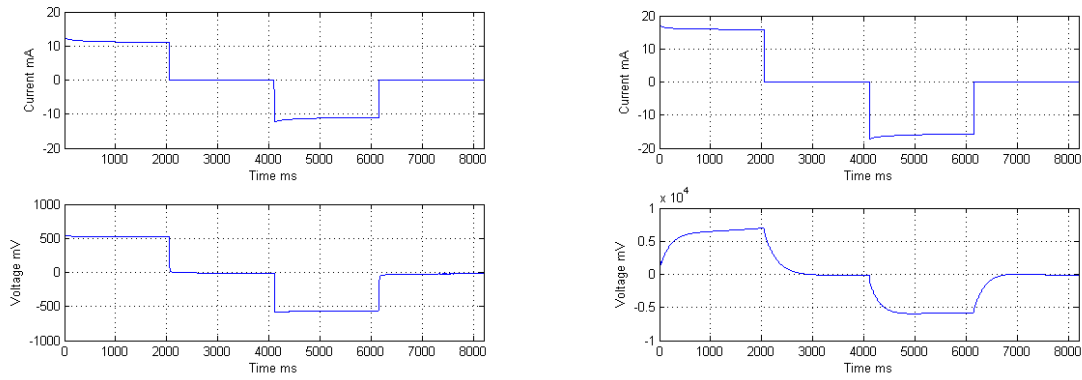
Figure 4.5: Waveform examples from L3 of injection current and voltage response without (left) and with (right) IP and other distortion effects from L3
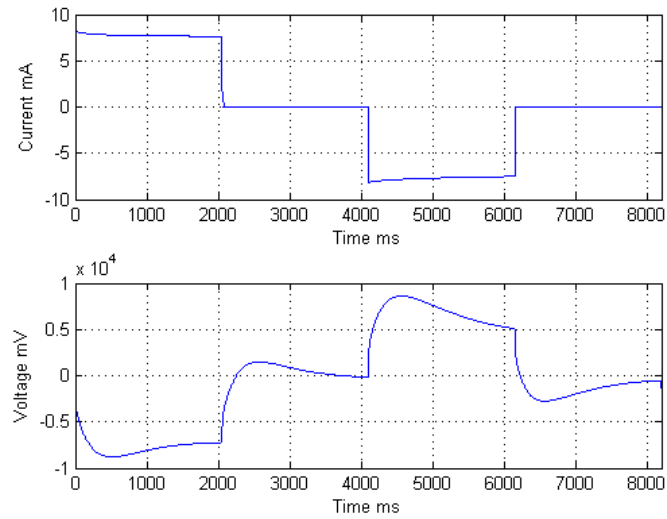
Figure 4.6: Waveforms of injection current and reversed voltage response with IP effect from voltage reversal zone at 50m of L3
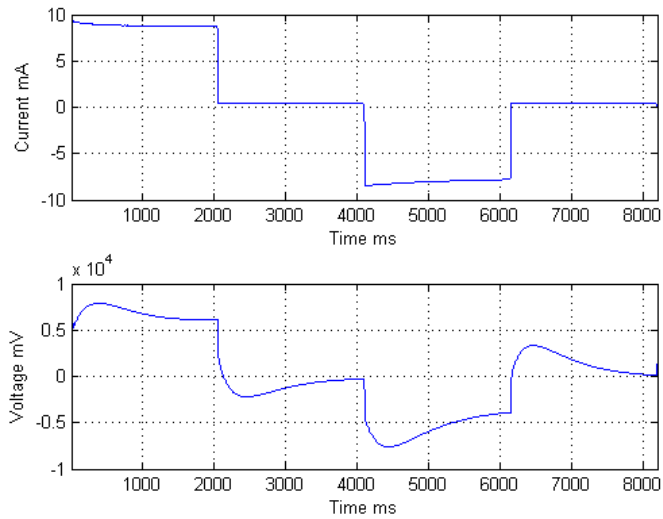
Figure 4.7: Waveforms of injection current and voltage response with IP effect of reversed polarity

Figure 4.8: Apparent resistivity (left) and chargeability (right) pseudo-section along BR1 (Schlumberger array). Resistivity is in $log_{10}(\Omega m)$. Chargeability is in mV/V. Electrode spacing is 8m

half. The chargeability pseudo-section of BR3 shows two strongly chargeable zones at about 120m and 180m along the borehole, in which the 120m one locates at similar location as previously discussed voltage reversal zone (4.6). The two anomalies can be responses from the same lithology.

4.3   Cross-boreholes

Cross-BR1-BR2 resistivity and chargeability tomography are shown in Figure 4.11 and 4.12. The resistivity tomography recovers a conductive anomaly between BR1 and BR2 and the anomaly extends to BR2. Also, BR1 gets into conductive materials at the end the borehole. These features are also suggested by single-borehole surveys (Figure 4.8, 4.9). However, cross-borehole tomography provides more information on the spatial distribution of different anomalies. The chargeability tomography suggests that the materials between BR1 and BR2 have a small chargeability variation while lithology around the middle of BR1 is more chargeable than that of around BR2. This feature is not captured by the

Figure 4.9: Apparent resistivity (left) and chargeability (right) pseudo-section along BR2 (Schlumberger array). Resistivity is in $log_{10}(\Omega m)$. Chargeability is in mV/V. Electrode spacing is 8m
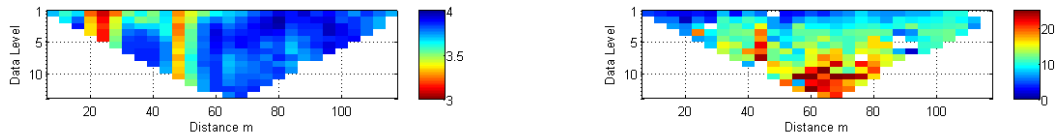

Figure 4.10: Apparent resistivity (left) and chargeability (right) pseudo-section along BR3 (Schlumberger array). Resistivity is in $log_{10}(\Omega m)$. Chargeability is in mV/V. Electrode spacing is 16m

Figure 4.11: Resistivity tomography between BR1(Left) and BR2(right) in $log_{10}(\Omega m)$. Electrode spacing is 8m

Figure 4.12: Chargeability tomography between BR1(Left) and BR2(right) in mV/V. Electrode spacing is 8m

Figure 4.13: Resistivity tomography between BR1(Left) and BR2(right) in $log_{10}(\Omega m)$. Data is acquired with dipole-dipole array $AM-NB$. Electrode spacing is 8m
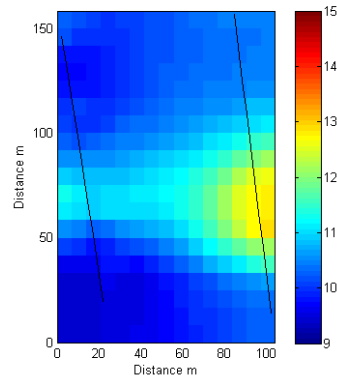
Figure 4.14: Chargeability tomography between BR1(Left) and BR2(right) in mV/V. Data is acquired with dipole-dipole array $AM-NB$. Electrode spacing is 8m

single-borehole measurement.

BR1-BR2 tomography data were also collected with another type of dipole-dipole array $AM-NB$, in which the positions of current and potential electrodes in the second borehole are switched. The results are shown in Figure 4.13 and 4.14. Although with anisotropy of earth materials and potential noise in the field measurement, the resistivity tomography result from $AM-NB$ array gives almost identical resistivity distribution pattern as that of from $AM-BN$ array with slightly difference in amplitude. This confirms the modelling result from the previous chapter. However, the chargeability tomography shows a rather different chargeability distribution. It is suggested that, instead of BR1, BR2 experience more chargeable lithology in the middle of the borehole. Similar feature is also noted by comparing single-borehole chargeability pseudo-sections of the two boreholes. This suggests that the $AM-NB$ array may be a more reliable array in imaging chargeability distribution while provide similar resistivity results as the $AM-BN$ array.

Tomography results between BR1 and BR3 (Figure 4.15, 4.16) show a conductive anomaly at the end of BR2, a chargeable anomaly between the end of BR1 and BR2 and another one around the top
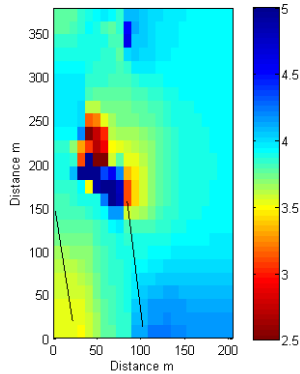
Figure 4.15: Resistivity tomography between BR1(Left) and BR3(right most) in $log_{10}(\Omega m)$. BR2 is also plotted for reference. Electrode spacing is 16m. BR3 is the edge of the image at 200m
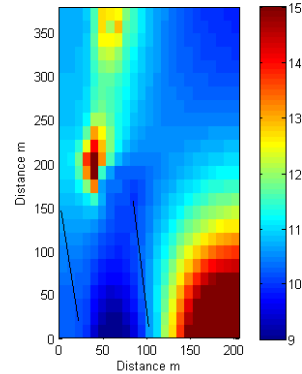
Figure 4.16: Chargeability tomography between BR1(Left) and BR3(right most) in mV/V. BR2 is also plotted for reference. Electrode spacing is 16m. BR3 is the edge of the image at 200m

of BR3. However, both resistivity and chargeability tomography fail to recover the details between BR1 and BR2 as in the BR1-BR2 tomography(Figure 4.11, 4.14). Moreover, it shows no coincidence with resistivity and chargeability anomalies observed in pseudo-sections along BR1 and BR3 (Figure 4.8 and 4.10). Referring to Figure 3.20, it is speculated that, compared with borehole separation, the dimensions of anomalies between BR1 and BR3 is too small to be delineated by cross-borehole array $AM - BN$.

4.4   Surface-to-surface

Similar as cross-borehole measurement, the $AM - BN$ array was also applied between surface lines. The data is inverted in the same way as cross-borehole data though a half-space geometry factor is used in calculating the apparent resistivity. The results are shown from Figure 4.17 and 4.20. In Figure 4.17, two conductive bands across L1 and L2 are observed. This coincides with the two conductive bands in the pseudo-sections of L1 and L2 and suggests that each of the two bands are connected across L1 and L2. Chargebility tomography suggests a chargeable zone between the end of L1 and L2. This result shows that array $AM - BN$ is applicable to surface lines and is capable of near surface tomography at proper line separation. It is useful in mapping the connectedness of near surface anomalies. However, the depth of investigation remains to be investigated.

For cross-L1-L3 tomography measured at a greater separation, resistivity and chargeability tomography both only show anomalies associated with each line with little detail in between. Also, it fails to recover details between L1 and L2 as observed in the L1-L2 tomography (Figure 4.19, 4.18). Similar as the case of BR1-BR3 tomography, the missing of details is likely because the size of anomalies is too small comparing with the separation between L1 and L3.

4.5   3D reconstruction

Figure 4.21 gives a 3D reconstruction of resistivity and chargeability distribution with surface-to-surface, cross-borehole tomography and surface line pseudo-sections. It clearly shows that each the two conduc-
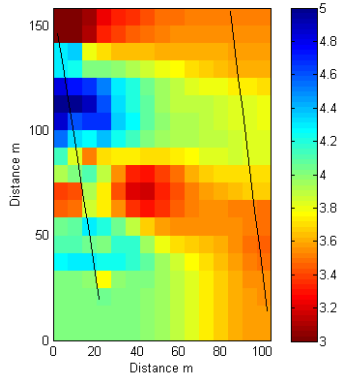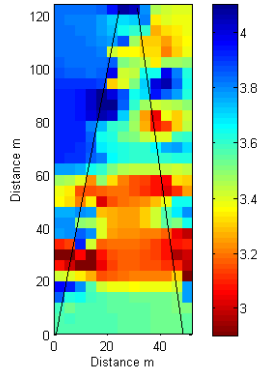
Figure 4.17: Resistivity tomography between L1(Left) and L2(right) in $log_{10}(\Omega m)$. Electrode spacing is 4m
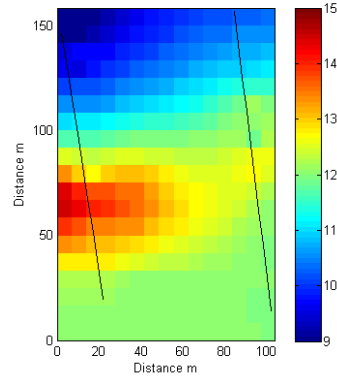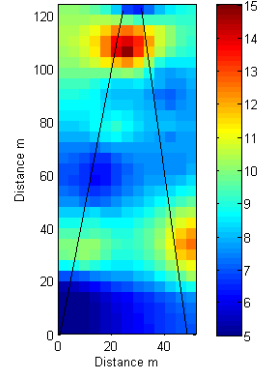

Figure 4.18: Chargeability tomography between L1(Left) and L2(right) in mV/V. Electrode spacing is 4m
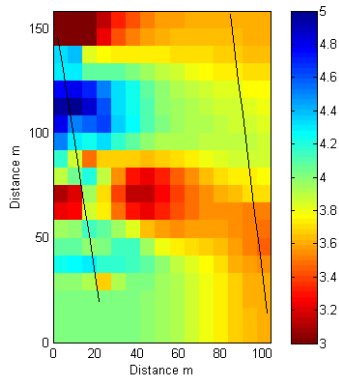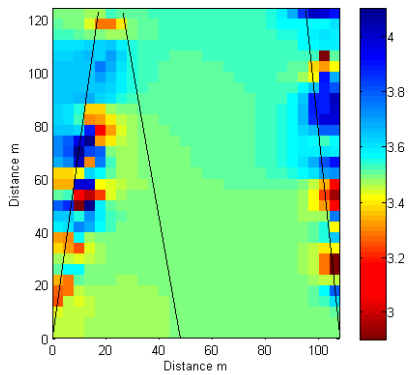

Figure 4.19: Resistivity tomography between L1(Left) and L3 (right most) in $log_{10}(\Omega m)$. Electrode spacing is 4m
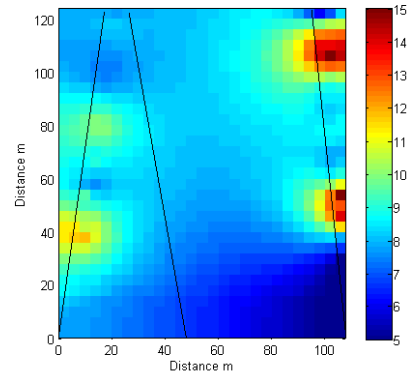
Figure 4.20: Chargeability tomography between L1(Left) and L3 (right most) in mV/V. Electrode spacing is 4m
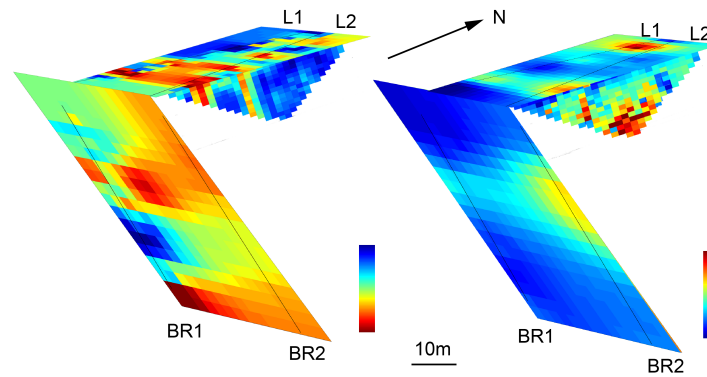
Figure 4.21: 3D fence diagram of resistivity (left) and chargeability (right) distribution around L1, L2 and BR1, BR2

tive bands shown both in L1 and L2 pseudo-sections are connected across the lines. The two bands extends to certain depth and may be responsible for the conductive anomaly between BR1 and BR2. The chargeability diagram shows that the chargeable band in at some depth of the L2 pseudo-section may be correlated with the chargeable zone recovered by L1-L2 tomography. This suggests that the surface-to-surface survey offers some depth of investigation as the chargeable band is not captured until the fourth level of Schlumberger array of L2. Another changeability anomaly between the end of L1 and L2 is suggested by L2 pseudo-section but not by that of L1. This suggest that the chargeable zone is restricted between the two lines and only extends to a shallow depth.

4.6 Surface-to-borehole

Surface-to-borehole tomography surveys were also conducted with $AM - BN$ array where AM is shifted along surface lines and BN is shifted along the boreholes. The electrode spacing of the surface line is 4m while the electrode spacing along borehole is 16m. However, the inversion programs available for use (Res2Dinv, Res3Dinv) require a uniform electrode spacing for tomography inversion. Therefore, the surface-to-borehole data could not be inverted at this moment. Instead, the apparent resistivity and chargeability across the surface line and the borehole are presented in Appendix B.

4.7 Discussion

With a combination of cross-borehole, surface-to-surface, and surface-to-borehole DC/IP tomography surveys, one is able to construct three-dimensional resistivity and chargeability distribution images of the surveyed area. Compared with conventional 3D DC/IP survey taken with surface grids, it offers better depth-constrained tomography results while data acquisition time is much reduced. At one of the expected mineralization zones, non-causal voltage responses are obtained. Such responses are further discussed in Appendix C and can be mapped and quantified by cross-correlation coefficient of waveforms of injected current and measured voltage response.
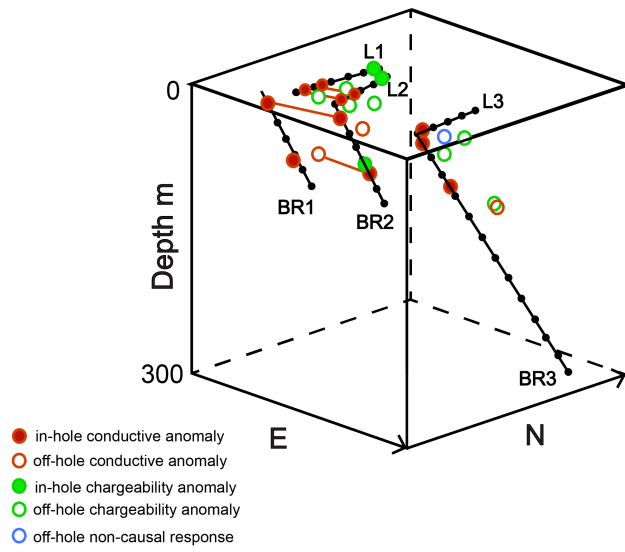
Figure 4.22: 3D view of various anomaly distrition with respect to the acquistion configuration

Chapter 5

Discussion and Conclusions

The DC resistivity and induced polarization responses of earth materials are not only determined by the electrical properties of the lithology, but are strongly influenced by presence of stress, pore space and fluid contents. As measurements taken in boreholes provide good repeatability over conventional surface arrays, borehole DC/IP imaging can be a powerful tool for monitoring time lapse changes in geotechnical and environmental studies. Also, for DC/IP surveys taken for mineral exploration purposes under a stressed environment, extra care should be taken in interpretation as the anomaly may be also due to stress anomaly or fluid filled structures.

For near surface borehole DC/IP surveys, the geometry factor plays an important role in accounting for the deviation effect and transition from half-space to full-space as the electrode array is shifted from the top to the bottom of the borehole. It is found that deviation and transition effects are both depth and dipping angle dependent. They are especially important for shallow dipping boreholes, in which case the difference in apparent resistivity calculated with and without correct geometry factors remains above typical data noise level throughout the boreholes. Such difference can be problematic in accurately imaging potential target structures. Therefore, for near surface borehole DC/IP surveys, rather than assuming a vertical borehole and/or full-space setting, the exact locations of electrode arrays should be obtained so that correct geometry factors can be applied for apparent resistivity calculation. Moreover, for cross-borehole DC/IP surveys, the geometry factor of certain array configuration may behave near singularly when the borehole separation is smaller than the current-potential electrode spacing. Data obtained with such arrays should be avoided in order to avoid introducing artifacts in tomography inversion. Alternatively, dipole-dipole array $AM - NB$ can be used. It offers similar detectability and its geometry factor is free of singularity issue. For current electrodes A and B in separate boreholes, the maximum of horizontal field is reached when the current-potential electrode separation is $\sqrt{2}$ times the borehole separation, at which the target can be best detected.

For underwater DC/IP surveys, a modified geometry factor is proposed to account for presence of the water layer. At the water-earth interface, more currents tend to flow into the water layer as the water is usually less resistive than sediments. However, with presence of conductive materials in the sediments such as clays and iron oxides, current may also tends to flow in the sediments side. The modified geometry factor requires estimates of resistivity of the water as well as the underlying half-space and is simple to be programmed for apparent resistivity calculation. It has been applied to resistivity data acquired with underwater configuration, where the water is more conductive than the sediments

and tends to bring down overall apparent resistivity. It effectively removes the low resistivity layer on the top of the pseudo-section, which is mostly affected by the water layer. Moreover, for time lapse DC/IP monitoring surveys associated with water, the temperature-resistivity variation of water also has a strong impact on resistivity data and should be well accounted. By applying different temperature-conductivity relationships reported in the literature to repeated resistivity measurements taken in the summer and the winter, the simple linear temperature-conductivity relationship is found to be more effective in temperature correction than the viscosity-based relationship (Appendix A).

Compared with single-borehole DC/IP surveys, cross-borehole DC/IP tomography provides directional and depth constrained spatial image of resistivity and chargeability distribution between boreholes. It greatly assists more rigorous and quantitative interpretation than using curving fitting and pseudo-sections. As geological features are three dimensional, cross-borehole DC/IP tomography is not only imaging the electrical properties in the plane of the boreholes, but may also be strongly influenced by off-hole targets. Cross-borehole tomography with surface boreholes at Sudbury North Range suggest that all three boreholes intersect a chargeability anomaly. However, after comparing with single-borehole pseudo-sections, it is concluded that the anomaly is likely to be due to an off-hole target. Therefore, although cross-borehole tomography has the advantage of providing 2D spatial distribution of imaged area, it should be combined with single-borehole surveys for accurate interpretation. In addition, environmental monitoring surveys, such as tracer experiments, are generally not recommended to be conducted close to background anomalies. The responses from tracer may manifest with background anomalies even though the anomalies are not in the same plane to be imaged.

A 2D color scheme is proposed for DC/IP tomography display. Using this color scheme, resistivity and chargeability data can be displayed on the same image and lithology associated with different resistivity-chargeability combinations can be directly differentiated by different colors in the color scheme. Rather than comparing two sets of data side by side, it enables direct visual examination of resistivity-chargeability variation pattern of the imaged area. This new color scheme can also be used to display other geophysical data, such as V_p and V_s, NMR and porosity, stress and V_p, to better characterize lithological changes and to investigate the correlation between two parameters.

Modeling results are calculated with different cross-borehole arrays for a conductive sphere between boreholes. It is shown that, although different in acquisition geometry, dipole-dipole arrays $AM - BN$ and $AM - NB$ give identical apparent resistivity responses. This modeling results is confirmed by cross-borehole resistivity tomography results from the exploration site at Canadian Malartic Mine, although with anisotropy of the Earth materials and potential noise in the field measurements. However, the two arrays give different chargeabilty tomography results across the same area. Considering the electrode separation is 16m at each measurement, the difference in chargeability tomography may be due to the fact that the current electrodes of one of the two arrays happen to have more contact with different parts of chargeable materials. With the sphere model, identical responses are also obtained with dipole-pole arrays $AM - B$ and $AM - N$. Moreover, dipole-pole arrays generally offer greater detectability than dipole-dipole arrays. Therefore, in case of small background noise for remote electrode, pole-dipole array is recommended for geotechnical and environmental monitoring surveys. It is also found that, for an off-hole anomaly, it is the borehole separation with respect to the dimension of the anomaly, rather than the resistivity contrast between the anomaly and the homogeneous half-space that plays the primary role that determines the detectability of the anomaly. In general, one should not expect to get effective responses from the anomaly in the middle of the two boreholes when the borehole separation is more

than two times greater than the dimension of the anomaly.

A combination of cross-borehole, surface-to-surface, and surface-to-borehole DC/IP were conducted at an exploration site of Canadian Malartic Mine in order to construct three-dimensional images of resistivity and chargeability distributions and to give DC/IP characterization of a gold mineralization system. At one of the expected mineralization zones, various non-causal voltage responses are obtained in a systematic manner, including voltage discharge while the current is being injected, voltage and induced polarization responses with reversed polarization. Such responses are obtained around the same expected mineralization zone and thus are unlikely to be due to instrumental errors. Some models have been proposed to explain such non-causal responses (Appendix *C*). However, the exact physical causes or complexity introduced by 3D heterogeneity of geology remain to be investigated.

Comparing with conventional 3D DC/IP surveys taken with surface grid, cross-borehole and surface-to-borehole surveys provide better depth constraint imaging while reducing data acquisition time. In addition, with presence of near surface anomalies, surface-to-surface tomography is found to be a useful tool to map the connectedness of these near surface anomalies. Due to limitation of inversion algorithm currently available, the surface-to-borehole dataset cannot be inverted. However, 3D resistivity and chargeability distribution images are able to be constructed by combining surface-to-surface, cross-borehole tomography results and surface line pseudo-sections. In addition to delineating a known mineralization zones with surface expressions, several anomalies are identified as potential mineralization zones.

Chapter 6

Outlook/Recommendations

Based on numerical modeling and field experiment results, the following actions and recommendations are proposed

1. Repeated single-borehole DC/IP measurement will be conducted on both 1300 and 1700 levels at the deep mine at Sudbury East Range. The correlation between potential changes in resistivity and stress will be investigated. In addition, the applicability of induced polarization effect in time lapse monitoring under a stressed environment will be discussed.

2. Cross-borehole DC/IP surveys will be taken with surface boreholes at Sudbury North Range at different offsets. The detectability and changes in resolution of DC/IP tomography at different borehole separation will be examined.

3. More sophisticated inversion algorithms are required to invert surface-to-borehole data taken at the exploration site of Canadian Malartic Mine. Then more complete 3D resistivity and chargeability images can be obtained across the surveyed area. The DC/IP results will also be combined with geological information to give geophysical and geological characterization of the gold mineralization system at Canadian Malartic Mine.

4. More research, both numerical modeling and laboratory experiment, is recommended to better understand the physical causes of voltage and IP response with reversed polarity as observed in the measurements at the exploration site of Canadian Malartic Mine.

5. DC/IP measurements on cores samples are required to give the DC/IP characterization of different lithology. Then single-borehole and cross-borehole imaging results can be more accurately interpretative in terms of real geology.

Appendices

Appendix A

Temperature-electrical resistivity correction for water related DC resistivity monitoring

The electrical conductivity of water is controlled by the combination of total dissolved solid and the temperature (Chang et al., 1983; Millero, 2001). The general conductivity-temperature relationship is complicated and non-linear (Millero, 2001). However, in the range of 0 to 30 °C for environmental monitoring, a linear and a viscosity-based equations are commonly used to represent the relation (Sorensen & Glass, 1987)

$$\sigma(t) = \sigma(25)[1 + \epsilon(t - 25)] \tag{A.1}$$

where $\sigma(t)$ is electrical conductivity at temperature t in °C; ϵ is temperature compensation factor and is recommended to be 0.0187 for natural waters (Hayashi, 2004).

$$\sigma(t) = \sigma(25)(\mu_t/\mu_{25})^{-b} \tag{A.2}$$

where $log\frac{\mu_t}{\mu_{25}} = \frac{A(25-t)-B(25-t)^2}{t+C}$, u_t is viscosity of water at temperature t °C, $\mu_{25} = 0.0008903 Nsm^{-2}$, $A = 1.1278$, $B = 0.001895$ °C^{-1}, $C = 88.93$ °C (Hayashi, 2004; Korson et al., 1969). Then the electrical resistivity is simply the inverse of electrical conductivity.

The percentage of change relative to resistivity at 0 °C based on Equation $A.1$ and $A.2$ is depicted in Figure $A.1$. In general, resistivity of water decreases with increasing temperature. However, Equation $A.1$ suggests a higher degree of variation compared with that of suggested by Equation $A.2$.

On Ogilvie's lake, Deep River, Ontario, repeated DC resistivity surveys across the lake have been conducted both in the summer and winter. The water layer is about 2m in thickness and has a significant impact on the first few levels of the data as the electrode spacing is 4m. In the winter, holes were drilled on the frozen lake so that electrodes could be put in contact with lake water. The change in resistivity inversion results due to change in resistivity of water can be clearly observed in Figure $A.2$. The inversion results of data collected in the winter collaboratively unveil a relatively resistive top layer, which is primarily caused by decrease in temperature of lake water.
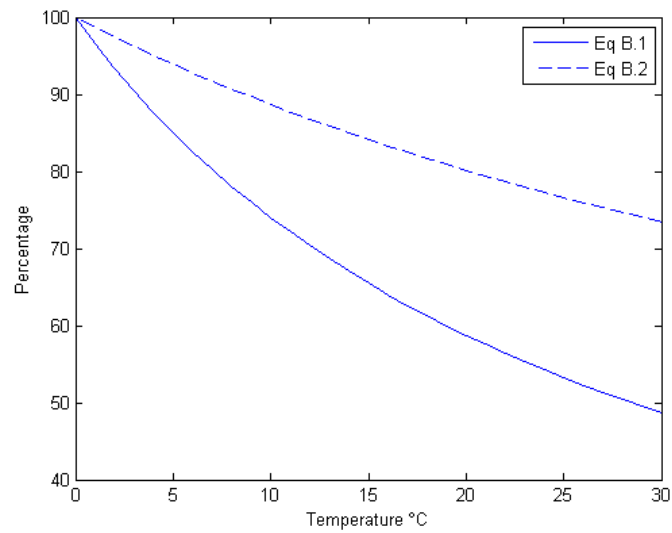
Figure A.1: Percentage of change in electrical resistivity from 0 to 30 °C based on Equation *A*.1 and *A*.2
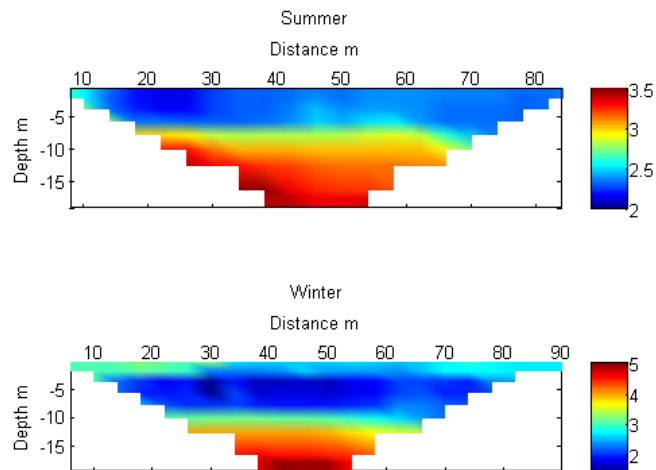
Figure A.2: Inverted resistivity pseudo-section of line 4 on Ogilvie's lake in the summer (top) and in the winter(bottom). The array type is Schlumberger and electrode spacing is 4m
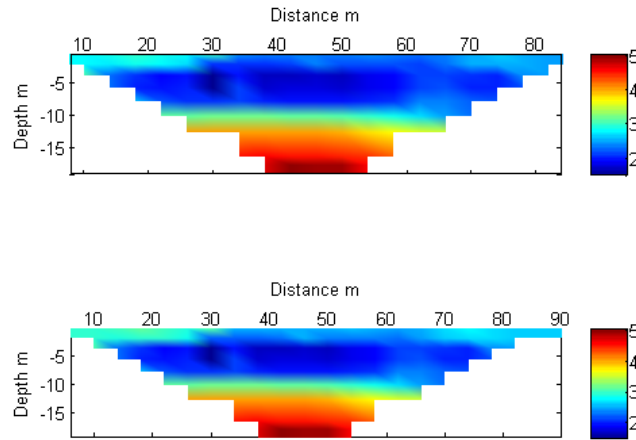
Figure A.3: Modified inverted resistivity pseudo-section of line 4 on Ogivile's lake in the winter based on Equation A.1 (top) and A.2 (bottom)

.

Equation $A.1$ and $A.2$ are both used to correct for temperature-resistivity variation of water. From 0°C to 25 °C, the percentage of change is 47% and 24% respectively. The modified results are shown in Figure $A.3$. By visual inspection, the top 5m in the modified resistivity pseudo-section using Equation $A.1$ is more uniform than that of using Equation $A.2$. Previous researchers have suggested that the conductivity-temperature relation is primarily controlled by change in viscosity of water and the viscosity-based equation should offers a higher accuracy than the linear relation(Robinson & Stokes, 1965; Korson et al., 1969; Sorensen & Glass, 1987; Hayashi, 2004). However, application of both equations to DC resistivity field examples on Ogilvie's lake suggests that Equation $A.1$ is more effective in correcting temperature based resistivity variation.

Appendix B

Surface-to-borehole

Due to limitation of the inversion program currently available for use (Res2Dinv, Res3Dinv), the surface-to-borehole tomography data from the exploration site at Canadian Malartic Mine could not be inverted. Instead, the apparent resistivity and chargeability across the surface line and the borehole are presented and discussed below. The distances along the two axes are the positions of the middle of AM or BN. All surface-to-borehole tomography surveys were also conducted with $AM - BN$ array where AM is shifted along surface lines and BN is shifted along the boreholes. The electrode spacing of the surface line is 4m while the electrode spacing along borehole is 16m. The distances along the two axes are the positions of the middle of AM or BN.

The L1-to-BR1 apparent resistivity result shows two conductive zones when AM is at around 20m, 50m and the two zones remains conductive and the one at 20m gets more chargeable as BN is shifted along BR1. This confirms the previous conclusion that the two conductive bands, shall extend towards BR1. A third conductive zone is shown at around 100m of L1. This is also a chargeable zone which extends along BR1. Similar features can be observed in the L2-to-BR1 survey. The apparent resistivity of L2-to-BR1 clearly shows the three conductive zones while the distances along L2 are consistently being shifted by about 10m. It shows that of conductive zone at 30m at L2 end is more chargeable than that of at the L1 end while the the conductive zone at 110m is less chargeable.

However, similar features are not observed in results from L2-to-BR2 or L1-to-BR2 surveys. As a matter of facts. it seems that both the resistivity and chargeability data is strongly contaminated by noise.

The L1-to-BR3 survey again shows three conductive zones at around 30m, 60m and 100m of L1 and these zones, remains conductive while BN is being shifted along BR3. However, the 30m and 100m zones, especially the 100m one, become much less conductive than the 60m. However, it is suggested that the 60m zone is associated with low chargeability while the 100m zone is associate with high chargeability. These two zones may both be mineralization zones however are associated with different lithology and/or different in concentration. Similar features are also observed in L3-to-BR3 survey and are likely to be caused by same mineralization as in previous mentioned surface-to-borehole surveys. However, the 30m zone becomes mostly non-chargeable and 60m zone does not start until BN is at 100m along BR3. This suggests that, from west to east, the the mineralization becomes less chargeable and the top gets deeper into the Earth.

Figure B.1: Apparent resistivity along L1 and BR1 in $log_{10}(\Omega m)$

Figure B.2: Chargeability along L1 and BR1 in mV/V

Figure B.3: Apparent resistivity along L2 and BR2 in $log_{10}(\Omega m)$

Figure B.4: Chargeability along L2 and BR2 in mV/V

Figure B.5: Apparent resistivity along L1 and BR2 in $log_{10}(\Omega m)$

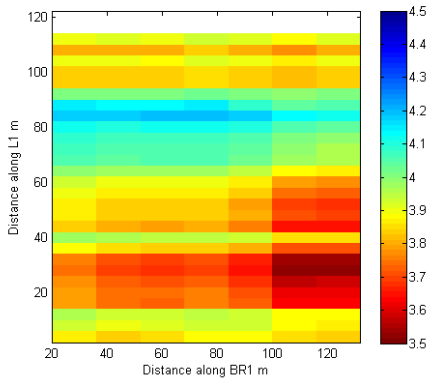**Figure B.6:** Chargeability along L1 and BR2 in mV/V

Figure B.7: Apparent resistivity along L2 and BR1 in $log_{10}(\Omega m)$
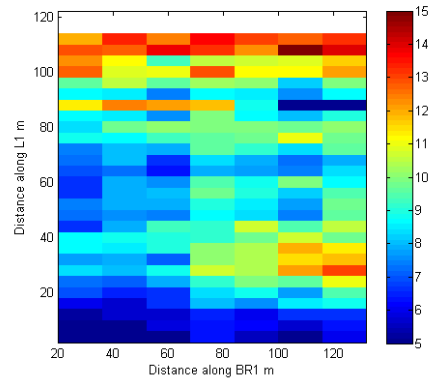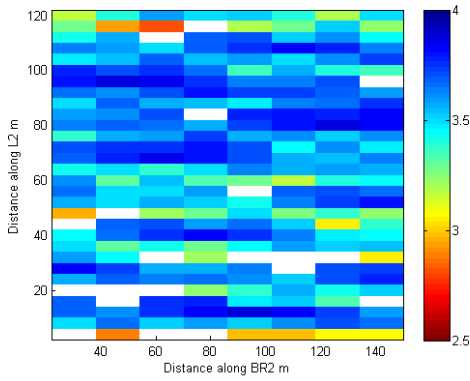

Figure B.8: Chargeability along L2 and BR1 in mV/V

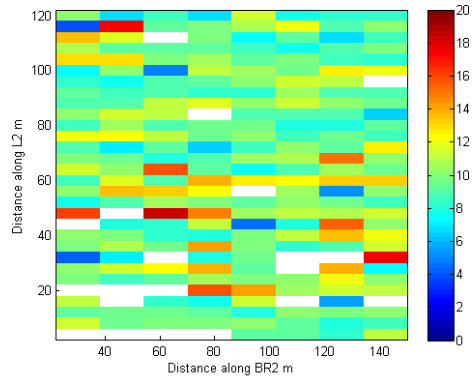**Figure B.9:** Apparent resistivity along L3 and BR3 $log_{10}(\Omega m)$

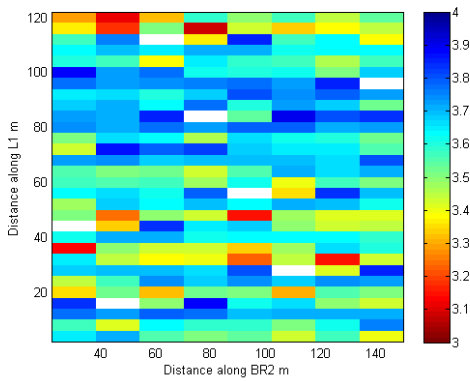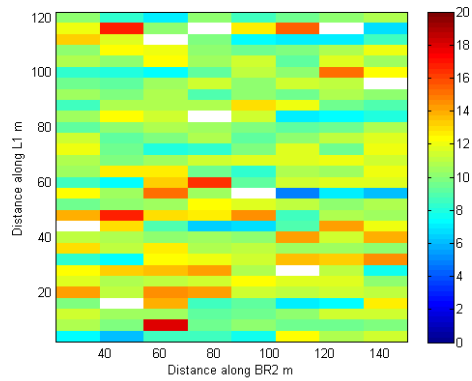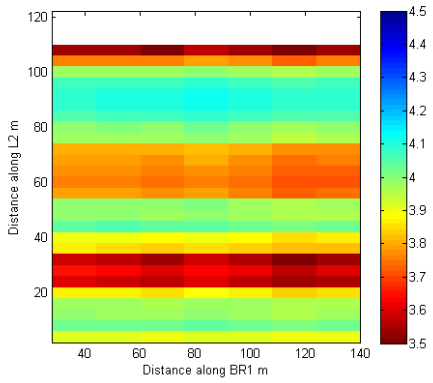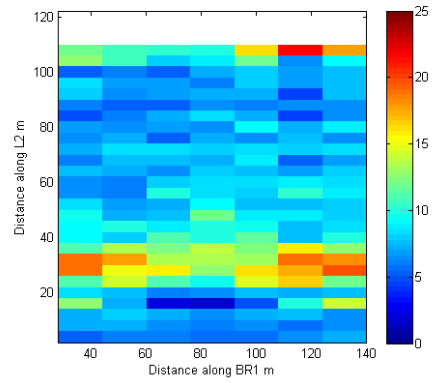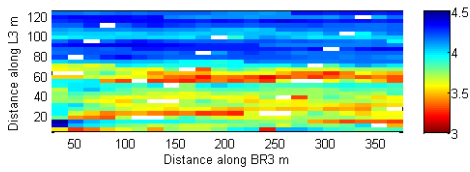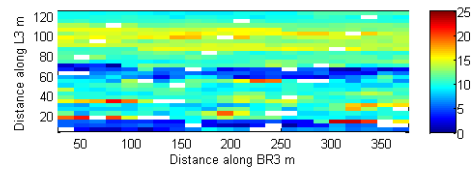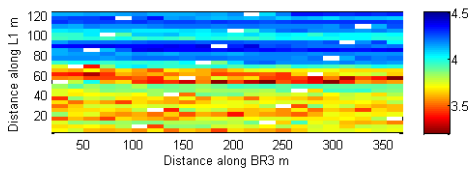**Figure B.10:** Chargeability along L3 and BR3 in mV/V

Figure B.11: Apparent resistivity along L1 and BR3 $log_{10}(\Omega m)$
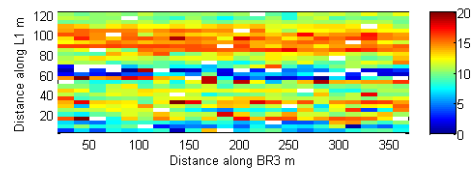

Figure B.12: Chargeability along L1 and BR3 in mV/V

Appendix C

Suggested models for non-causal voltage responses

In the DC/IP survey along surface line L3 at the exploration site of Canadian Malartic Mine, voltage and IP responses with reversed polarity were obtained as seen in Figure 4.6, 4.7. These responses are measured systematically from one of the expected mineralization zones that has been mapped by the geologists and are unlikely to be due to instrumental errors. As illustrated in Figure C.1 a, for a $AMNB$ array in a homogeneous full-space, the potential from M to N decreases when current is injected at A. Then $\Delta V = V_M - V_N$ has the same polarity as current injection at A. If the material is chargeable, ΔV firstly keeps increasing during current-on time and then decays back to 0 during current-off time. However, in the vertical negative apparent resistivity zone, it is found that the polarity of voltage response is reversed with respect to the injection current. Figure 4.6 shows a waveform example of such phenomenon. When $+I$ is injected at A, instead of getting positive response as in Figure 4.5, negative voltage response is measured. Such reversed voltage response is measured again when current is injected at B. One possible explanation for such non-causal phenomenon is illustrated in Figure C.1 b. Due to disturbance of conductive materials, when $+I$ is injected at A, potential at N is higher than potential at M and therefore negative ΔV is measured. Another possibility is illustrated in Figure C.2. In a 3D Earth, the injected current initially flows at some azimuth with respect to the profile being measured. Then it flows in a circular pattern towards the profile through some chargeable materials (simplified as a capacitor) and finally sinks at the other current electrode. Then negative voltage response will be measured at one side the of current flow circle. Also, when the current is switched off, the capacitor acts as a current source. The current flows in a regular pattern so that IP effect with a opposite polarity with respect to the on-time voltage response is obtained. It is also noted that the voltage firstly increases to maximum and then decreases during current-on time. Similar voltage decay pattern is also measured around the voltage reversal zone (Figure 4.7). One possible layered Earth model responsible for such phenomenon is illustrated in Figure C.3. The first layer of the Earth is represented as a capacitor and the following layers as resistors in parallel with the capacitor. The injected current first flows through the capacitor so that the voltage response increases. Then, the current flows into subsequent layers which act as resistors. For a parallel configuration, the current tends to flow through resistors rather than the capacitor and, by Ohm′s law, the measured voltage decreases. However, the exact cause also remains to be investigated.

a)

b)
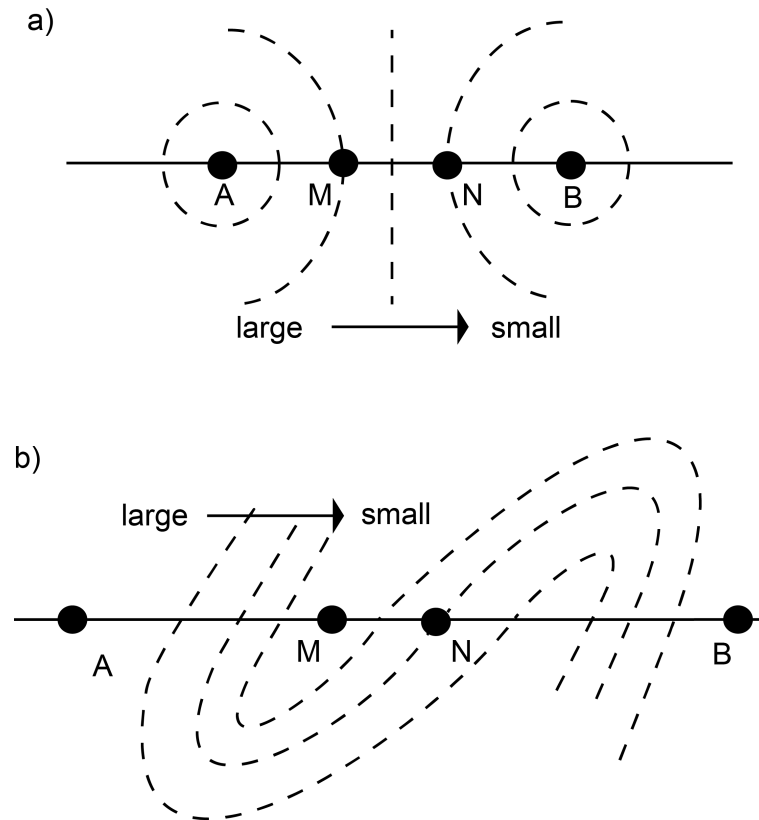
Figure C.1: Schematic plots of equipotentials (dashed lines) of array $AMNB$. a(top) in a homogeneous full-space; b(bottom) disturbed by resistivity anomaly and give reversed voltage response

The cross-correlation coefficient at zero time lag of the current and voltage waveforms $\Phi(\tau = 0)$ can be used to quantify such distortion effects. Without IP and other distortion effects, Φ is close to 1. Its deviation from 1 indicates the degree of distortion of the voltage response from the injected current. As depicted in Figure C.5, the Φ pseudo-section clearly recovers the chargeability anomalies as in Figure C.4. However, in case of NRS170100 where the chargeability anomaly does not coincide with the resistivity anomaly, the Φ pseudo-section gives slightly different anomaly distribution pattern from either the apparent resistivity or chargeability pseudo-sections. For L3 survey, Φ gets close to -1 in the voltage reversal zone. Also, it recovers the chargeability anomaly at the bottom of the pseudo-section.

One advantage of using the Φ parameter over chargeability is that it is less affected by presence of self-potential. However, the quantitative relationship between Φ and the other two parameters remains to be established.
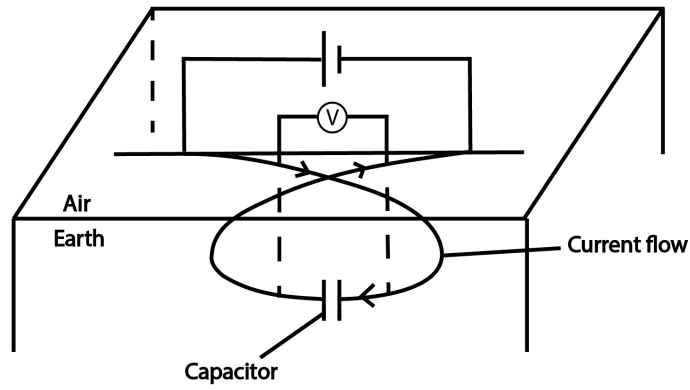
Figure C.2: Schematic plots of a capacitor with reversed current flow in a 3D Earth
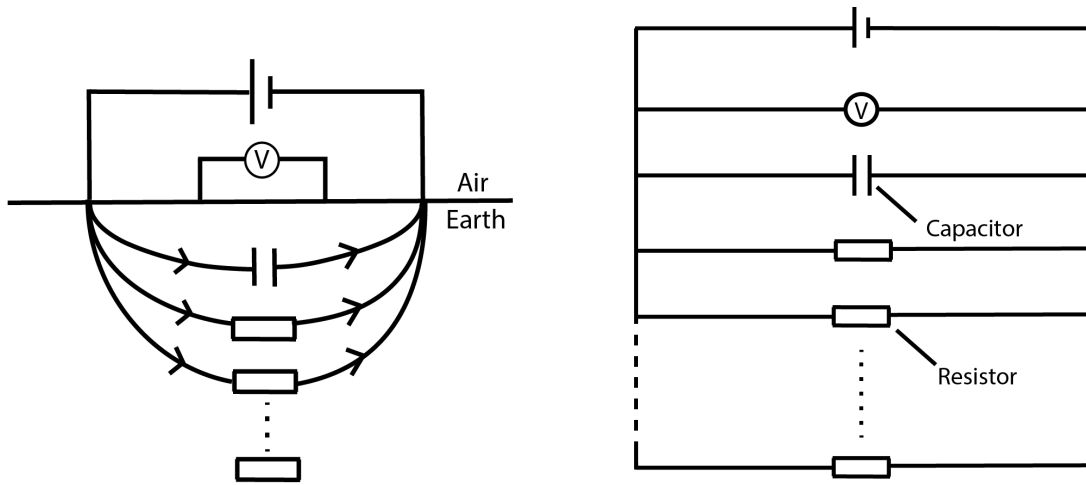
Figure C.3: Simplified circuit digram representing the layered Earth materials as a capacitor in parallel with resistors

Figure C.4: Apparent resistivity in $log10(\Omega m)$(left), chargeability in mV/V (right) pseudo-sections of NRS170143
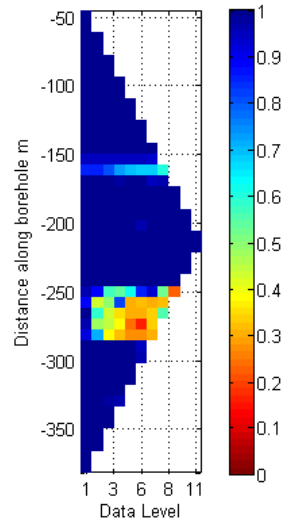
Figure C.5: Cross-correlation coefficient pseudo-section of NRS170143
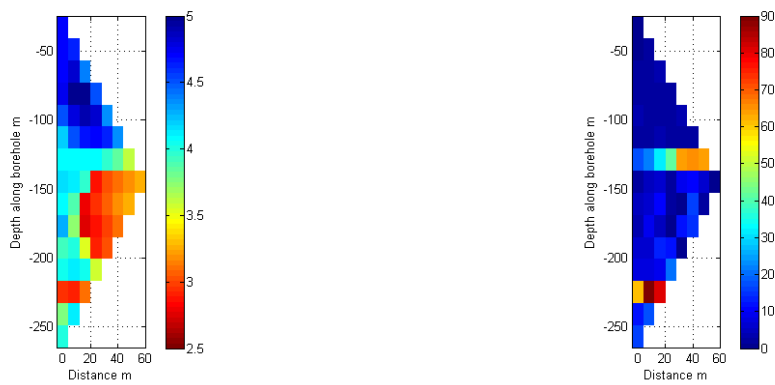
Figure C.6: Apparent resistivity in $log10(\Omega m)$ (left), chargeability in mV/V (right) pseudo-sections of NRS170100
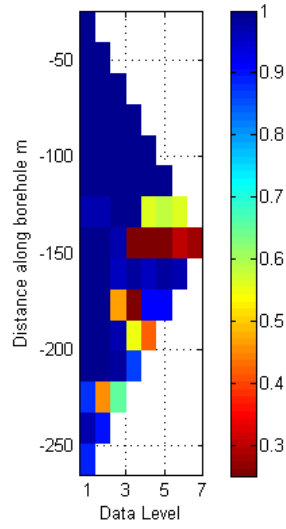
Figure C.7: Cross-correlation coefficient pseudo-section of NRS170100
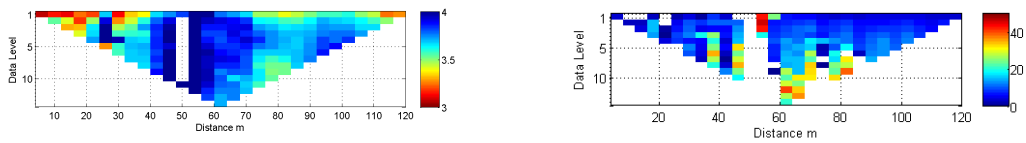
Figure C.8: Apparent resistivity in $log10(\Omega m)$ (left), chargeability in mV/V (right) pseudo-sections of L3
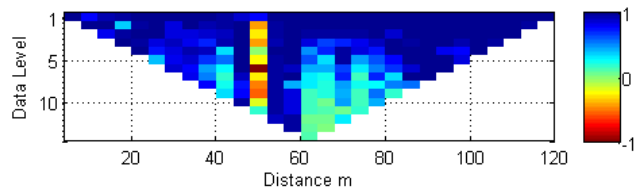
Figure C.9: Cross-correlation coefficient pseudo-section of L3

Bibliography

Archie, G, E., 1942, The electrical resistivity log as an aid in determining some reservoir characteristics, *Petroleum Transactions of AIME*, **146**, 54–62.

Asch, T. & Morrison, H. F., 1989, Mapping and monitoring electrical resistivity with surface and subsurface electrode arrays, *Geophysics*, **54**(2), 235–244.

Asfahani, J., 2005, Directional borehole logging configurations using dc and telluric methods for detecting deep conductors not intersected by wells, *Pure and Applied Geophysics*, **162**(12), 2523–2556.

Baumgartner, F., 1996, A new method for geoelectrical investigations underwater, *Geophysical Prospecting*, **44**(1), 71–98.

Bevc, D. & Morrison, H. F., 1991, Borehole-to-surface electrical resistivity monitoring of a salt water injection experiment, *Geophysics*, **56**(6), 769–777.

Binley, A. & Kemna, A., 2005, Dc resistivity and induced polarization methods, in *Hydrogeophysics. Water and Science Technology Library 50*, edited by R. Yuram & S. Hubbard, pp. 129–156, Springer,New York, USA.

Bleil, D., 1953, Induced polarization, a method of geophysical prospecting, *Geophysics*, **18**(3), 636–661.

Brace, W. F. & Orange, A., 1968a, Electrical resistivity changes in saturated rocks during fracture and frictional sliding, *Journal of Geophysical Research*, **73**(4), 1433–1445.

Brace, W. F. & Orange, A., 1968b, Further studies of the effects of pressure on electrical resistivity of rocks, *Journal of Geophysical Research*, **73**(16), 5407–5420.

Brace, W. F., Orange, A., & Maden, T., 1965, The effect of pressure on the electrical resistivity of water-saturated crystalline rocks, *Journal of Geophysical Research*, **70**(22), 5669–5678.

Budak, B., Samarskii, A., & A.N., T., 1964, *A collection of problems on Mathematical Physics*, Macmillan, New York, USA.

Cardarelli, E. & Filippo, G., 2009, Electrical resistivity and induced polarization tomography in indentifying the plume of chlorinated hydrocardbons in sedimentary formation: a case study in rho (milan-italy), *Water Management and Research*, **27**, 595–602.

Chang, C., Sommerfeldt, T. G., & Schaalje, G. B., 1983, Relationships of electrical conductivity with total dissolved solid and cation concentration of sulfate-dominant soil extracts, *Canadian Journal of Soil Science*, **63**, 79–86.

Daily, W., Ramirez, A., Binley, A., & LaBrecque, D., 2005, Electrical resistance tomography-theory and practice, in *Near-surface geophysics*, edited by D. Butler, pp. 525–550, Society of Exploration Geophysicists, Tulsa, Okla, USA.

Daniels, J., 1983, Hole-to-surface resistivity measurements, *Geophysics*, **48**(1), 87–97.

Daniels, J. & Dyck, A., 1984, Borehole resistivity and electromagnetic methods applied to mineral exploration, *IEEE Transactions on Geoscience and Remote Sensing*, **GE-22**, 80–87.

Daniels, J. J., 1977, Three-dimensional resistivity and induced polarization modelling using buried electrodes, *Geophysics*, **42**(1), 1006–1019.

Daniels, J. J., 1978, Interpretation of buried electrode resistivity data using a layered earth model, *Geophysics*, **43**(5), 988–1001.

Dines, K. & Lytle, R. J., 1979, Computerized geophysical tomography, in *in Proceedings of IEEE*, vol. 67, pp. 1065–1073.

Gallas, J. D. F., Taioli, F., & Filho, W. M., 2011, Induced polarizaiton, resistivity, and self-potential: a case history of contamination evaluation due to landfill leakage, *Environmental Earth Sciences*, **63**(2), 251–261.

Ghorban, A., Cosenza, P., Ruy, S., Doussan, C., & Florsch, N., 2008, Non-invasive monitoring of water infiltration in a silty clay loam soil using spectral induced polarization, *Water Resources Research*, **44**, W08402.

Glover, P., 2009, What is the cementation exponent? a new interpretation, *The Leading Edge*, **28**(1), 82–85.

Glover, P., 2010, A generalized archieâĂŹs law for n phases, *Geophysics*, **75**(6), E247–E265.

Glover, P. W., Hole, M., & Pous, J., 2000, A modified archieâĂŹs law for two conducting phases, *Earth and Planetary Science Letters*, **180**(3), 369–383.

Hallof, P. G., Yamashita, C. M., Wynn, J. C., Grosz, A. E., Carlson-Foscz, V. L., Witherly, K. E., ., & Reynolds, J., 1990, *Induced polarization applications and case histories*, SEG.

Hayashi, M., 2004, Temperature-electrical conductivity relation of water for environmental monitoring and geophysical data inversion, *Environmental monitoring and assessment*, **96**(1-3), 119–128.

Jamtlid, A., Magnusson, K. A., Olsson, O., & Stenberg, L., 1984, Electrical borehole measurements for the mapping of fracture zones in crystalline rock, *Geoexploration*, **22**(3), 203–216.

Kate, J. M., 1994, Shear and resistivity behaviour of sandstones, in *in proceedings of the 7th IAEG Congress*, vol. 2, pp. 889–897, Lisbon, Portugal.

Keller, G. & Frischknecht, F. C., 1966, *Electrical Methods in Geophysics Prospecting*, Pargamon Press, Oxford.

Kemna, A., Binley, A., & Slater, L., 2004, Crosshold ip imaging for engineering and environmental applications, *Geophysics*, **69**(1), 97–107.

Kim, J. H., Yi, M. J., Park, S. G., & Kim, J. G., 2009, 4-d inversion of dc resistivity monitoring data acquired over a dynamically changing earth model, *The Journal of Physical Chemistry*, **68**(4), 522–532.

Korson, L., Drost-Hansen, W., & Millero, F. J., 1969, Viscosity of water at various temperatures, *The Journal of Physical Chemistry*, **73**(1), 34–39.

LaBrecque, D., Ramirez, A., Daily, W., Binley, A., & Schima, S., 1996, Ert monitoring of environmental remediation processes, *Meas. Sci. Technol.*, **7**(375), E247–E265.

Li, Y. & Oldenburg, D., 2000, 3d inversion of induced polarization data, *Geophysics*, **65**, 1931–1945.

Loke, M., 2001, Tutorial: 2-d and 3-d electrical imaging surveys, Copyright (1996-2012).

Loke, M. & Barker, R., 1996a, Rapid least-squares inversion of apparent resistivity pseudosections by a quasi-newton method, *Geophysics Prospecting*, **44**(1), 131–152.

Loke, M. & Barker, R., 1996b, Practical techniques for 3d resistivity surveys and data inversion, *Geophysics Prospecting*, **44**(3), 499–523.

Lytle, R., 1982, Resistivity and induced-polarization probing in the vicinity of a spherical anomaly, *Geoscience and Remote Sensing, IEEE Transactions on*, **GE-20**(4), 493–499.

Merkel, R. & Alexander, S., 1971, Resistivity analysis for models of a sphere in a half-space with buried current source, *Geophysics Prospecting*, **19**(4), 640–651.

Millero, F., 2001, *The physical chemistry of natural waters*, Wiley-Interscience, New York, USA.

Morse, P. M. & Feshbach, H., 1953, *Methods of Theoretical Physics*, vol. Part II, New York: McGraw-Hill.

Muller, K., Vanderborght, J., Englert, A., Kemna, A., Huisman, J. A., Rings, J., & Vereecken, H., 2010, Imaging and characterization of solute transport during two tracer tests in a shallow aquifer using electrical resistivity tomography and multilevel groundwater samplers, *Water resources research*, **46**(3), E247–E265.

Nimmer, R. E., Osiensky, J. L., Binley, A. M., Sprenke, K. F., & Williams, B. C., 2007, Electrical resistivity imaging of conductive plume dilution in fractured rock, *Hydrogeology Journal*, **15**(5), 877–890.

Olayinka, A. & Yaramanci, U., 2000, Use of block inversion in the 2-d interpretation of apparent resistivity data and its comparison with smooth inversion, *Journal of Applied Geophysics*, **45**, 63–81.

Oldenborger, G., Routh, P., & Knoll, M., 2005, Sensitivity of electrical resistivity tomography data to electrode position errors, *Geophysical Journal International*, **163**, 1–9.

Oldenburg, D. & Li, Y., 1994, Inversion of induced polarization data, *Geophysics*, **59**, 1327–1341.

Oldenburg, D. & Li, Y., 1999, Estimating depth of investigation in dc resistivity and ip surveys, *Geophysics*, **64**(2), 403–416.

Oldenburg, D., McGillivary, P., & Ellis, R., 1993, Generalized subspace method for large scale inverse problem, *Geophysical Journal International*, **114**, 12–20.

Osasan, K. S. & Afeni, T. B., 2010, Review of surface mine slope monitoring techniques, *Journal of Mining Science*, **46**, 177–186.

Osiensky, J. L., Nimmer, R., & Binley, A. M., 2004, Borehole cylindrical noise during holeâĂŞsurface and holeâĂŞhole resistivity measurements, *Journal of Hydrology*, **289**(1-4), 78–94.

Pun, W. & Milkereit, B., 2011, *Geophysical time series data from a stressed environment*, Master's thesis, University of Toronto.

Qian, W., Milkereit, B., McDowell, G., Stevens, K., & Halladays, S., 2007, Borehole resistivity logging and tomography for mineral exploration, in *in Proceedings of Exploration 07: Fifth Decennial International Conference on Mineral Exploration*, edited by B. Milkereit, pp. 1115–1118.

Ramirez, A., Daily, W., LaBrecque, D., Owen, E., & Chestnut, D., 1993, Monitoring an underground steam injection process using electrical resistance tomography, *Water Resource Research*, **29**(1), 73–87.

Robinson, R. & Stokes, R. H., 1965, *Electrolyte solutions*, Butterworth.

Schima, S., LaBrecque, D. J., & Lundegard, P. D., 1996, Monitoring air sparging using resistivity tomography, *Groundwater Monitoring and Remediation*, **16**(2), 131–138.

Schlumberger, C., 1920, *Etude sur la prospection electrique du sous-sol: Gauthier-Villar et Cie*, Paris, France.

Seigel, H. O., 1971, Some comparative geophysical case histories of base metal discoveries, *Geoexploration*, **9**, 81–97.

Seigel, H. O., Nabighian, M., Parasnis, D., & Vozoff, K., 2007, The early history of the induced polarization method, *The Leading Edge*, **26**(3), 312–321.

Shima, H., 1992, 2d and 3d resistivity imaging reconstruction using cross-hole data, *Geophysics*, **55**, 682–694.

Shirokova, V. L. & Ferris, F. G., 2013, Microbial diversity and biogeochemistry of a shallow pritine canadian shield groundwater system, *Geomicrobiology Journal*, **30**, 140–149.

Slater, L. D. & Sandberg, S. K., 2000, Resistivity and induced polarization monitoring of salt transpot under natural hydraulic gradients, *Geophysics*, **65**(2), 408–420.

Sorensen, J. A. & Glass, G. E., 1987, Ion and temperature dependence of electrical conductance for natural waters, *Analytical Chemistry*, **59**(13), 1594–1597.

Summer, J., 1976, *Principle of induced polarization for geophysical exploration*, Elsevier Scientific Pub. Co.

Telford, W. M. & Sheriff, R. E., 1990, *Applied geophysics*, vol. 1, Cambridge university press.

Tsourlos, P., Ogilvy, R., Papazachos, C., & Meldrum, P., 2011, Measurement and inversion schemes for single borehole-to-surface electrical resistivity tomography surveys, *Journal of Geophysics and Engineering*, **8**(4), 487.

Van, N. R., 1953, Limition on resistivity methods as inferred from the buried sphere problem, *Geophysics*, **18**, 423–433.

Van, N. R. & Cook, K. L., 1966, *Interpretation of resistivity data*, U.S. Government, Washington DC, USA.

Ward, S., 1990, Resistivity and induced polarization methods, in *Geotechnical and environmental geophysics. Society of Exploration Geophysics*, vol. 1, Society of Exploration Geophysicists, Tulsa, Okla, USA.

Webb, J., 1931, Potential due to a buried sphere, *Phys.Rev.,*, **37**, 292–302.

Yi, M., Kim, J., & Son, J., 2009, Borehole deviation effect in electrical resistivity tomography, *Geosciences Journal*, **13**(1), 87–102.

Zhou, B. & Greenhalgh, S. A., 1997, A synthetic study on crosshole resistivity imaging using different electrode array, *Exploration Geophysics*, **28**, 1–5.

Zhou, B. & Greenhalgh, S. A., 2000, Cross-hole resistivity tomography using different electrode configuration, *Geophysical Prospecting*, **48**(5), 887–912.

Zonge, K., Wynn, J., & Urquhart, S., 2005, Resistivity, induced polarization, and complex resistivity, in *Near-surface geophysics*, edited by D. Butler, pp. 265–300, Society of Exploration Geophysicists, Tulsa, Okla, USA.